

ICE GENESIS

Creating the next generation of 3D simulation means for icing

Type of action: Research and Innovation Action

Call identifier: H2020-MG-2018-SingleStage

Topic: MG-2-5-2018 Innovative technologies for improving aviation safety and certification in icing conditions

Deliverable D10.4

Public synthesis of snow icing physics models and tools improvements

EC Grant Agreement number: 824310

Start date of project: 1 January 2019

Duration: 60 months

Lead beneficiary of this deliverable:

ONERA

Due date of deliverable: 30/09/2022

Actual submission date: 01/03/2024

Version #: R1.0

Project funded by the European Commission within the H2020 Programme (2014-2020)		
Type		
R	Document, report excluding the periodic and final reports	X
DEM	Demonstrator, pilot, prototype	
DEC	Websites, patents filing, press & media actions, videos, etc.	
OTHER	Software, technical diagram, etc.	
ETHICS	Ethics requirement	
ORDP	Open Research Data Pilot	
Dissemination level		
PU	PUBLIC, fully open, no embargo e.g. web	X
PU+E1	PUBLIC after embargo of 12 months from date of publication	
PU+E3	PUBLIC after embargo of 3 years after the project's end	
RE	RESTRICTED, only for certain members of the consortium (including the Commission Services): specify here which consortium members have access to the document	
CO	CONFIDENTIAL, only for members of the consortium (including the Commission Services)	
CO+IGAB	CONFIDENTIAL, only for members of the consortium (including the Commission Services) and for the ICE GENESIS Advisory Board	

Revision History

V #	Date	Description / Reason of change	Author
R0.0	6/10/23	Initial version	ONERA
R1.0	23/12/2023	Version submitted to the reviewers	ONERA, TUDA
R1.1	08/02/24	Version corrected following reviewers remarks	ONERA

Deliverable Contributors

Authors

Organisation	Authors' name	Export control status date	Export control status
ONERA	O. Rouzaud Q. Duchayne	11/10/2018	No data subject to export control data

Contributors

Organisation	Authors' name	Export control status date	Export control status
AIH	F. Dezitter B. Aguilar	07/03/2022	No data subject to export control
AIT	A. Zanon	19/12/2023	No data subject to export control
ONERA	Q. Duchayne O. Rouzaud	11/10/2018	No data subject to export control
POLIMI	M. Gallia G. Gori A. Guardone	15/12/2022	No data subject to export control
TUDA	K. Köbschall J. Hussong I. Roisman	16/06/2021	No data subject to export control

Export Control Status

Author / Contributor	Type of data	Position in document of concerned text/data*	Jurisdiction and ECCN under this jurisdiction	Status of authorization
AIH	Experimental data, Computational data, Scientific publications	4.1, 4.2	Not subject to Export Control Regulation	Not Applicable
AIT	Experimental data	4.2, 5	Not subject to Export Control Regulation	Not Applicable
ONERA	Experimental data, Computational data, Scientific publications	4.1, 4.2, 5, 7	Not subject to Export Control Regulation	Not Applicable
POLIMI	Computational data, Scientific publications	4.2, 7	Not subject to Export Control Regulation	Not Applicable
TUDA	Experimental data, Computational data, Scientific publications	4.1, 4.2, 7	Not subject to Export Control Regulation	Not Applicable

****To be checked by the Owner of the document before delivery of the document!***

Internal Reviewers

Organisation	Internal Reviewers' name
AIRBUS HELICOPTER	F. Dezitter
GENERAL ELECTRIC AEROSPACE	P. Vanacore

Table of Contents

1	Glossary.....	7
2	Executive summary.....	8
3	Introduction	9
4	Experimental and modelling activities.....	10
4.1	Snowflake transport.....	10
4.1.1	Drag.....	10
4.1.2	Melting.....	15
4.2	Snowflake impact.....	20
4.2.1	Impact regime threshold.....	20
4.2.2	Shattering.....	22
4.2.3	Accretion	23
5	Snow numerical capability in the 3D numerical tools	31
6	Conclusions	33
7	Annex	34
7.1	TUDA snowflake free fall experiment.....	34
7.2	TUDA and IAG snowflake melting experiment	35
7.3	Current HAIC sticking and erosion models	36
7.4	Sensitivity numerical results to the measurement uncertainties.....	38
7.5	Optimization study - RTA cases TP07, TP08 and TP09.....	39
8	Bibliography	40

Table of Tables

Table 1: Experimental data of CSTB ice accretion experiment with snow conditions	24
Table 2: Experimental data of RTA ice accretion tests with snow conditions	25
Table 3: Experimental and geometrical data for the snowflake free fall experiments	34
Table 4: Experimental data of snowflake melting	35

Table of Figures

Figure 1: Snow phenomena description	9
Figure 2: Exemplary digital models of snowflakes showing the variety of the generated snowflakes	10
Figure 3: Experimental set-up for drag measurement [7]	10

Figure 4: Digital model of a snowflake and the corresponding convex hull enclosing it.....	11
Figure 5: Models of a simple convex hull and its projection. Left: three-dimensional element of the convex hull, approximated by a tetrahedron. Right: projection of the triangle ABC on an arbitrary plane. Definition of the inclination angle α and the projection length S	11
Figure 6: Evaluation of the main geometrical properties of the shapes of the digital snowflakes from the Monte Carlo computational simulations compared with the theoretical predictions	12
Figure 7: Comparison of fall speeds obtained for the artificial snowflake data set with the data set [8] gathered with natural snow.....	12
Figure 8: Oblate and prolate spheroid geometries.....	13
Figure 9: Probability density function of the ratio A_{\perp}/A_{\parallel} of the area A_{\perp} projected onto a plane normal to the relative velocity vector to the area A_{\parallel} projected onto a parallel plane. [7]	13
Figure 10: Drag models assessment. Left: drag coefficient comparison.	15
Figure 11: Left: snowflake production system consisting of a humid air supply, wires as nucleation sites and a funnel for aggregation. Middle: laboratory produced snowflakes [15]. Right: natural snowflakes [16]	15
Figure 12: Melting process. Left: experimental setup for observation of melting of a laboratory produced snowflake. Right: melting process of an exemplary snowflake	16
Figure 13: Melting process. Left: comparison of the reduced diameter vs. the reduced time. Right: comparison of the experimental and numerical melting times for both Mitra's and mNS models [15]	18
<i>Figure 14: Comparison between experimental and numerical results for the snowflake melting time</i>	19
Figure 15: Comparison between experimental and numerical results for the snowflake melting time computed with IGLOO2D, CEDRE/SPIREE and CEDRE/SPARTE.....	19
Figure 16: Sequence of aluminum target impact onto a levitated snowflake at 1 m/s	20
Figure 17: Dimensionless parameter $\xi = UnD_{min}^2/3/\beta$ vs. the length scale ratio D_{min}/D_{max} (AIT data in red and blue markers; TUDA data in black and magenta markers; solid ice particles data in green Hauk et al. [6])	21
Figure 18: Example of the post-processing procedure of one snowflake impact video. Left: tracked objects with their red and yellow ID labels. Right: visualization of the individual particle trajectories	22
Figure 19: Averaged number density histogram of the generated fragments after snowflake impact	22
Figure 20: Numerical ice shape for CSTB-Run405.....	25
Figure 21: Numerical ice shape for CSTB-Run905.....	25
Figure 22: Ice shape comparison for RTA-TP08	26
Figure 23: Ice shape comparison for RTA-TP09	26
<i>Figure 24: Sensitivity numerical results for Run403.....</i>	26
<i>Figure 25: Numerical sensitivity results</i>	27
Figure 26: Sensitivity to the measurement uncertainties for CSTB-Run405	28
Figure 27: Sensitivity to the measurement uncertainties for CSTB-Run905	28
Figure 28: Ice shape comparison using the optimal coefficients for CSTB-Run 403	29
Figure 29: Ice shape comparison using the optimal coefficients for CSTB-Run903	29
Figure 30: Ice shape comparison	29
Figure 31: Ice shape comparison	29
<i>Figure 32: Numerical ice thickness over the time obtained using the optimised HAIC models</i>	30
Figure 33: Ice shape comparison using the mean optimal coefficients for Run403.....	30
Figure 34: Ice shape comparison using the mean optimal for Run905	30

Figure 35: Left: comparison of the free fall velocities. Right: comparisons of melting times	31
Figure 36: Impacting collection efficiency – TP08.....	32
Figure 37: Ice shapes - TP08.....	32
Figure 38: Ice shape comparison for Run401	36
Figure 39: Ice shape comparison for Run901	36
Figure 40: Ice shape comparison for Run403	36
Figure 41: Ice shape comparison for Run903	36
Figure 42: Ice shape comparison for Run407	36
Figure 43: Ice shape comparison for Run907	36
Figure 44: Ice shape comparison for TP14.....	37
Figure 45: Ice shape comparison for TP15.....	37
Figure 46: Ice shape comparison for TP19.....	37
Figure 47: Ice shape comparison for TP20.....	37
Figure 48: Ice shape comparison for TP21.....	37
Figure 49: Ice shape comparison for TP22.....	37
Figure 50: Sensitivity numerical results for Run401	38
Figure 51: Sensitivity numerical results for Run901	38
Figure 52: Sensitivity numerical results for Run403	38
Figure 53: Sensitivity numerical results for Run903	38
Figure 54: Sensitivity numerical results for Run405	38
Figure 55: Sensitivity numerical results for Run905	38
Figure 56: Sensitivity numerical results for Run407	39
Figure 57: Sensitivity numerical results for Run907	39
Figure 58: ice shape comparison using mean optimal coefficients in HAIC models and initial HAIC models with the experiment for TP07	39
Figure 59: Ice shape using mean optimal coefficients in HAIC models and initial HAIC models with the experiment for TP08	39
Figure 60: Ice shape using mean optimal coefficients in HAIC models and initial HAIC models with the experiment for TP09	39

1 Glossary

Abbreviation / Acronym	Description/meaning
AIH	Airbus Helicopters
AIT	Austrian Institute of Technology GMBH
CSTB	Centre Scientifique et Technique du Bâtiment – French scientific and technical centre
HAIC	High Altitude Ice Crystal – European project on ice crystals
HS	Hölzer-Sommerfeld
HW	Heymsfield-Wetsbrook
IAG	Industrie Automatisierungsgesellschaft m.b.H. – Austrian company
LWR	Liquid Water Ratio
MMD	Median Mass Diameter
mNS	Modified Nusselt-Sherwood
ONERA	Office National de Recherche et d'Etudes Aérospatiale – French aerospace research centre
POLIMI	Politecnico di Milano – Italian research university
Pr	Prandtl number
ROnI	Region Of non Interest
Sc	Schmidt number
TUDA	Technische Universität Darmstadt – German research university
TWC	Total Water Content

2 Executive summary

The Deliverable D10.4 summarizes the activities conducted within the WP10 of the ICE-GENESIS project related to the snow numerical capabilities. Further details on the activities are given in the Deliverables D10.1 [1], D10.2 [2], D10.3 [3], including the description of the experimental, modelling and numerical activities. It is noteworthy to mention that these activities are tightly associated to those of the WP5 “Instrumentation for snow and microphysical properties” and WP7 “Snow test capability” and have led to a fruitful collaboration with the partners involved in these WPs.

Most of the efforts in WP10 have been devoted to the transport models and, more specifically, the drag and thermal models for snow particles. On the drag part, at first, several academic experiments have been performed within ICE-GENESIS considering real and artificial snowflakes in order to get the estimation of the free fall speed. The next step consisted in assessing and down-selecting several physical models versus this experimental data, using 2D numerical solvers. This led to retaining the Hölzer-Sommerfeld model [4]. On the thermal part, the same process has been employed and the down-selection process has led to retain an adaptation of the HAIC model [5] based on the melting time of a snow particle. In any case, for these two models, the geometrical description of the snow particle is based on the oblate spheroid approximation. An additional conclusion of the work is that 2D geometrical descriptors are relevant and could be also used. Both drag and thermal models have been implemented into the 3D numerical tools and successfully assessed with respect to the experimental data and the 2D numerical results.

On the accretion part, the HAIC models concerning the sticking efficiency and the erosion have been employed and assessed versus two experiments performed within ICE-GENESIS at CSTB and RTA IWTs on a NACA0012 airfoil. A first objective has consisted in evaluating the influence of the experimental uncertainties on the experimental LWR, TWC values on the numerical results. In a second time, an optimization process has been performed, trying to define optimal values for some parameters of the HAIC sticking and erosion models. The objective function of this process was based on the ice shape. While this process has been quite successful for most of the cases, the variations of the parameters are questionable from a physical point of view. Such a fact indicates that a better modelling is required or that the objective function used for the optimization process is not adapted.

Finally, some additional experimental and modelling activities have been realized to describe the snowflake impact. A model for the break-up threshold has been proposed and matched with the HAIC model for Ice Crystals [6]. The experimental data has also conducted to propose a probability density function describing the size of the snow particles emitted after an impact.

3 Introduction

This report Deliverable D10.4 summarizes part of the activities conducted within the WP 10 of the ICE-GENESIS project related to the snow numerical capabilities. The report focusses mostly on the description of the models and their assessment in the 2D and 3D numerical tools. Further details are given in the Deliverables D10.1 [1], D10.2 [2], D10.3 [3], including the description of the experimental activities. It is noteworthy to mention that these activities are tightly associated to those of the WP5 “Instrumentation for snow and microphysical properties” and WP7 “Snow test capability” and have led to a fruitful collaboration with the partners involved in these WPs. Figure 1 provides a synthetic description of several phenomena occurring during in-flight snow icing conditions. During the ICE-GENESIS project, attention has been put on the snowflake transport, impact and accretion phases, but with different types of approaches.

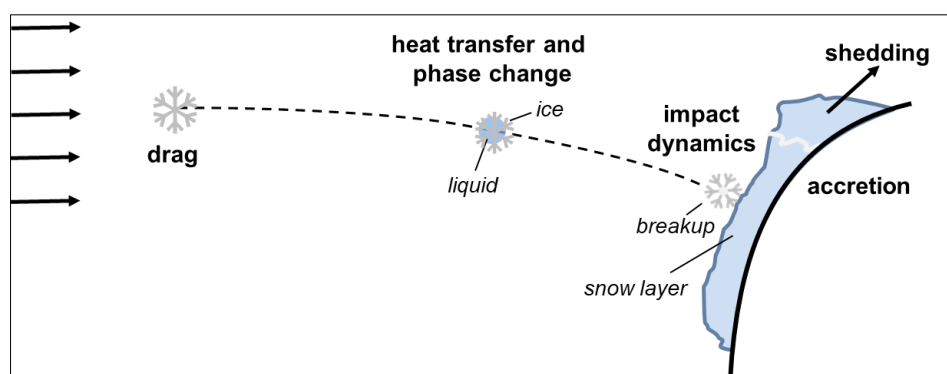


Figure 1: Snow phenomena description

The next chapter begins with the transport part. Experimental and modelling activities have enabled to derive several drag and melting models, to perform some preliminary assessment using 2D solvers, for instance, leading to a down-selection of one model for each phenomenon. The same process has been adopted for the snowflake impact described in the second section of the chapter, leading to a model for defining the impact threshold regime of break-up and another model for describing the size of the secondary particles after impact. The section 4.2.3 concerns the accretion part. In that case, no model has been derived, but existing ice crystals models developed in the framework of the HAIC project have been used to evaluate the influence of the measurement uncertainties of experiments performed within CSTB and RTA Wind Tunnels on the numerical results. Besides, an optimization method has also been developed to modify some of the coefficients of the accretion models (erosion and sticking efficiency phenomena). Finally, some activities have been done on uncertainty quantification techniques concerning ice accretion.

The fourth chapter is devoted to the implementation of the down-selected drag and thermal models in the 3D numerical tools and, more specifically, their assessment with respect to previous results obtained with the 2D numerical tools and some specific 3D configurations (2D extruded).

4 Experimental and modelling activities

4.1 Snowflake transport

4.1.1 Drag

4.1.1.1 Experimental study and snowflake geometric description

In this study, real and artificial snowflakes have been used to characterize their trajectories and to estimate the value of the drag coefficient. The artificial snowflakes have been produced by plastic additive manufacturing and their drag coefficients are obtained by measuring the terminal velocity in a liquid container, matching the Reynolds number typically encountered in natural occurrences [7]. Some examples of the shapes used in the experiments are shown in Figure 2. These shapes are similar to the snowflakes usually observed under natural conditions. While all snowflakes are composed of dendritic ice crystals, the number of monomers and the riming determined by the liquid water path have been varied.



Figure 2: Exemplary digital models of snowflakes showing the variety of the generated snowflakes

The experimental setup, shown in Figure 3 consists of a container filled with a glycerol–water mixture, cameras, light sources with diffusing sheets, a temperature sensor and the artificial snowflake. The snowflake is shown in Figure 3 once fixed at the bottom of the container prior to the experiment and once in the field of view of the cameras. The drag coefficient of the snowflake is estimated from the measurements of the snowflake terminal velocity by consideration of the balance of the buoyancy force, weight and drag force.

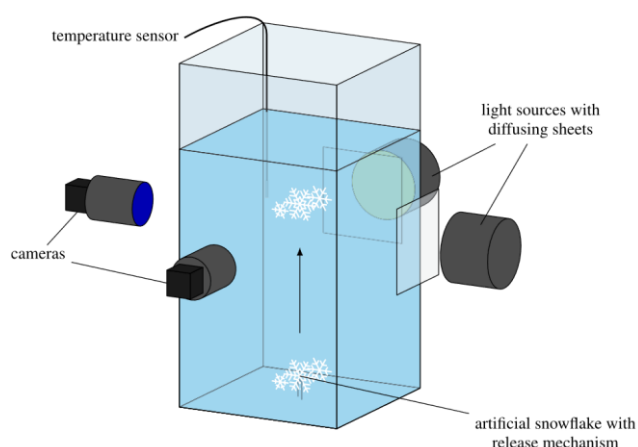


Figure 3: Experimental set-up for drag measurement [7]

Since it is unfeasible to accurately measure the three-dimensional geometries of natural snowflakes, the approximation with the convex hull provides a useful simplification. The main idea of the proposed approach is in the representation of the snowflake as a porous body, whose shape is a convex hull of the particle. An example of such a porous body is shown in Figure 4.

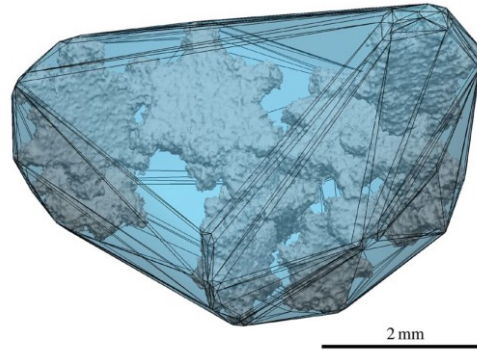


Figure 4: Digital model of a snowflake and the corresponding convex hull enclosing it

The drag coefficient of the snowflake can be modelled based on the correlation for the drag coefficient of the much simpler geometry of the convex hull shape. It is shown that the drag force applied to a snowflake and the drag force applied to the convex hull are approximately the same if the pressure loss due to the body porosity is small. This condition is satisfied if

$$\frac{d_{pore}^2 \varphi^3}{360 d^2 (1 - \varphi)^2} Re \ll 1$$

where d is the particle size, d_{pore} is the average pore size, φ is the particle porosity and Re is the Reynolds number based on the relative velocity of the surrounding gas. This condition is satisfied for most of the particles used in the experiments and for most cases of the real snow conditions.

Another topic of interest is to try to rebuild a three-dimensional geometric description of a snowflake from its 2D images. Since the shapes of the artificial snowflakes is more or less known, some correlations have been developed to estimate the most relevant three-dimensional descriptors to predict the drag of snowflakes from a two-dimensional projection onto an arbitrary plane. Transition from 2D images to 3D shapes is possible if a specific shape of the body is assumed. In order to generate bodies whose statistical properties can fit the measured distributions of the particle sphericities, a specific kind of 3D surfaces is generated. The elements of the surfaces are represented by triangles of the length L , as shown in Figure 5. The vertices of the triangle are located at the surface of a sphere of the radius R . These two parameters determine the variety of the forms of the assumed 3D bodies. The projected areas and the sphericities of these 3D bodies and their 2D projections on arbitrary directions can be computed from geometrical considerations, as shown schematically in Figure 5 right hand side. The details of the analysis of the geometry of such body can be found in [7].

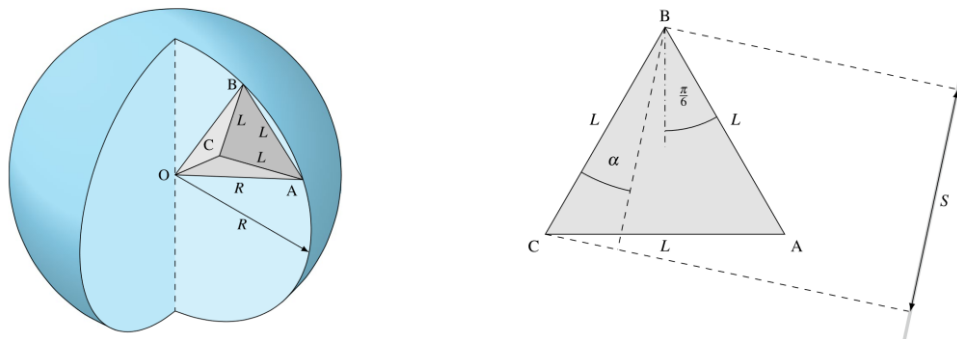


Figure 5: Models of a simple convex hull and its projection. Left: three-dimensional element of the convex hull, approximated by a tetrahedron. Right: projection of the triangle ABC on an arbitrary plane. Definition of the inclination angle α and the projection length S

The geometrical properties of the 3D figure have been compared with the properties of their projections in random direction. Clear correlations have been found for the equivalent particle

diameter and sphericity with the corresponding properties of the 2D projections [7]. The comparison of the geometry of theoretical shape with the shapes of the artificial snowflakes are shown in Figure 6. The agreement indicates that the method can be applied to the real meteorological particles.

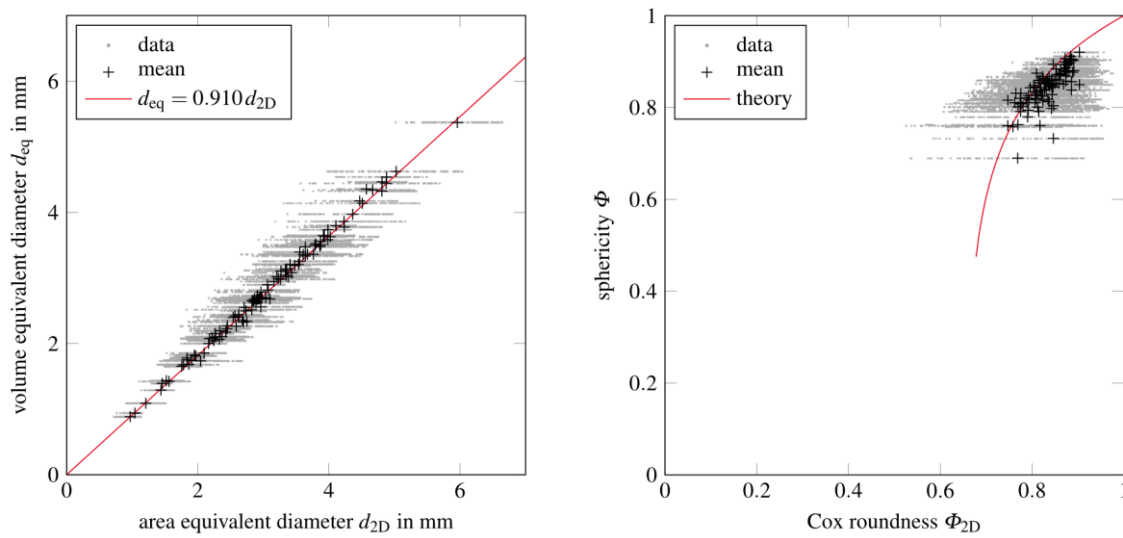


Figure 6: Evaluation of the main geometrical properties of the shapes of the digital snowflakes from the Monte Carlo computational simulations compared with the theoretical predictions

The correlation between fall speed and maximum dimension of the snowflake projection has been tested. With these quantities, the synthetic data can be compared with measurements obtained with natural snow. Since literature on the drag coefficients of natural snowflakes is sparse, the fall speed is used as an indirect measure of drag to validate the data. The experimental data for the fall speed are shown in Figure 7 in comparison with the theoretical predictions. The agreement is rather good, which indicated the validity of the method.

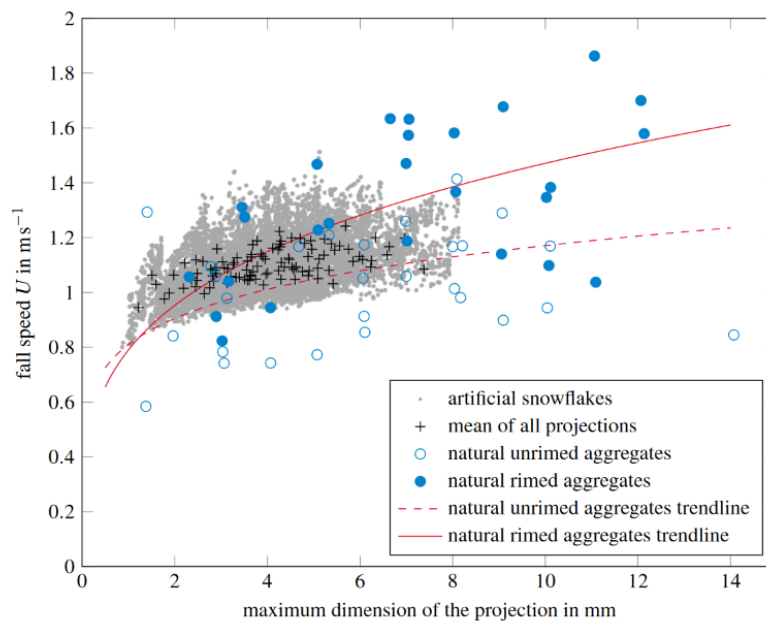


Figure 7: Comparison of fall speeds obtained for the artificial snowflake data set with the data set [8] gathered with natural snow

Another possible geometric description of the snowflakes relies on the oblate and prolate spheroid reconstructions. Indeed, thanks to 2D images of the snowflakes, an ellipse enclosing the particle shadow area can be determined. From the axes of the ellipse, one can construct either an oblate spheroid or a prolate spheroid. Please refer to [9] for more details. An example of these spheroids is available in Figure 8.

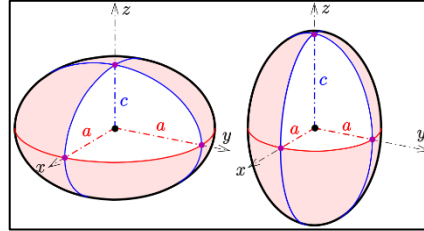


Figure 8: Oblate and prolate spheroid geometries

Using this spheroid reconstruction, the following parameters, useful for computing the drag coefficient, can be deduced as:

$$d_V = \left(\frac{6V_{\text{spheroid}}}{\pi} \right)^{1/3}, \quad \Phi = \frac{\pi d_V^2}{A_{\text{spheroid}}}, \quad \Phi_{\perp} = \frac{\pi d_V^2}{A^{\perp}}$$

where d_V is the volume equivalent diameter. The term A_{spheroid} denotes the surface of the approximated spheroid ($A_{\text{ref}} \equiv A_{\text{spheroid}}$) and A^{\perp} is the projected surface of the particle in the considered view ($A^{\perp} = \pi a^2$). A_{spheroid} can be defined in two different ways, depending on whether oblate or prolate spheroid (see Figure 8) is considered for the snowflake definition :

$$\begin{cases} A_{\text{spheroid}} = 2\pi a^2 + \pi \frac{c^2}{e} \ln \left(\frac{1+e}{1-e} \right) & \text{for oblate spheroid,} \\ A_{\text{spheroid}} = 2\pi a^2 \left(1 + \frac{c}{ae} \arcsin e \right) & \text{for prolate spheroid} \end{cases} \quad \text{with} \quad e = \sqrt{1 - \frac{c^2}{a^2}}$$

Finally, experiments show that the motion of the snowflakes leads to some preferable particle orientation. This is illustrated in Figure 9. The most probable orientation of the particle corresponds to $A_{\perp}/A_{\parallel} \approx 1.5$. This means that a particle rotation leads to the orientation of the largest projected area normal to the direction of the relative gas velocity. This result has to be taken into account when estimating the values of Φ_{\perp} and Φ in order to predict C_d .

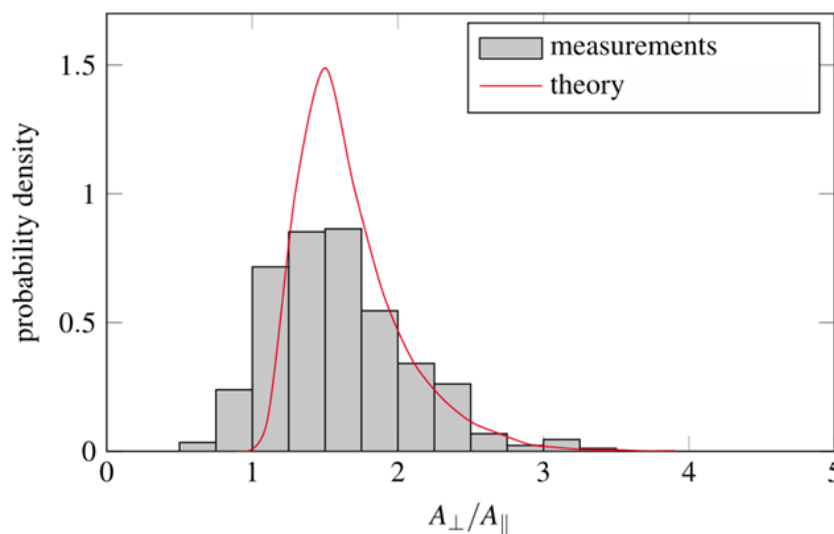


Figure 9: Probability density function of the ratio A_{\perp}/A_{\parallel} of the area A_{\perp} projected onto a plane normal to the relative velocity vector to the area A_{\parallel} projected onto a parallel plane. [7]

4.1.1.2 Numerical model

For the computation of the snow particle trajectory, the particle motion equation can read:

$$m_p \frac{dv_p}{dt} = F_D + m_p g \quad , \quad F_D = -\frac{1}{2} \rho_a \|w\| w A_{ref} C_{D,ref}(Re_p)$$

where m_p is the snow particle mass, v_p its velocity, F_D the drag force, g the gravity, ρ_a the air density and $w = v_p - v_a$ denotes the relative velocity between air and the particle. In the following, $\|w\|$ will simply be denoted w . The drag coefficient $C_{D,ref}$ is defined with respect to the reference surface A_{ref} . It is a function of the particle Reynolds number $Re_p = \frac{\rho_a w d_{ref}}{\mu_a}$ where μ_a is the air dynamic viscosity, d_{ref} a characteristic length scale and ρ_a the air density. Different models have been tested like Hölzer and Sommerfeld [4], Heymsfield and Westbrook [10], Haider and Levenspiel [11] and Ganser [12] models. Hereafter, we just simply describe the first two ones and the reader will refer to the articles for further details.

Two sets of definitions are used to define $C_{D,ref}$. They are presented in publications [9] and [13]. The first one is drawn from the Hölzer and Sommerfeld correlation for non-spherical particles [4] :

$$C_{D,ref} = \frac{8}{Re_p \sqrt{\Phi_{\perp}}} + \frac{16}{Re_p \sqrt{\Phi}} + \frac{3}{\sqrt{Re_p} \Phi^{0.75}} + \frac{0.42}{\Phi_{\perp}} 10^{0.4(-\log_{10} \Phi)^{0.2}}$$

where Φ and Φ_{\perp} are respectively the sphericity and the crosswise sphericity. The second set of definition is obtained from the Heymsfield and Westbrook model [10] :

$$C_{D,ref} = A_r^{1/2} C_{D0} \left[1 + \frac{\delta_0}{\sqrt{Re_p}} \right]^2 \quad \text{with } C_{D0} = 0.35 \text{ and } \delta_0 = 8$$

where the area ratio A_r is the ratio of the particle projected area to the area of a circumscribing circle

$$A_r = \frac{A^{\perp}}{\frac{\pi d_{max}^2}{4}}.$$

4.1.1.3 Preliminary assessment and down-selection – 2D numerical tools

Some comparisons have been done by both TUDA and ONERA, respectively on the drag coefficient and the free fall speed. In TUDA part, the models of Hölzer and Sommerfeld [4], Haider and Levenspiel [11] and Ganser [12] have been used and the geometrical description of the snowflake is based on the three-dimensional convex hull geometry as an input. The comparisons with the experimental drag coefficient [7] are rather satisfactory, see Figure 10. The best agreement is given by the HS model.

In ONERA part, preliminary validation have been done comparing the numerical results to the TUDA free-fall experiment data [9]. The models under consideration are the HS model [4] with either the oblate spheroid or the prolate spheroid geometrical description [13], and the Heymsfield and Westbrook model [10]. The operating conditions and snowflake parameters for the cases considered are described in Annex 7.1. As it can be seen in Figure 10 right hand side, a reasonable agreement between the numerical results obtained with the models and the experimental values is achieved. The models appear to have comparable accuracy, with a mean relative error around 25% for these cases.

As a conclusion, the HS model has been retained for snow conditions considering also the results obtained for ice crystals during the European project HAIC [14]. Moreover, based on the melting process down-selection described in the next section, we recommend to use the oblate spheroid geometric description.

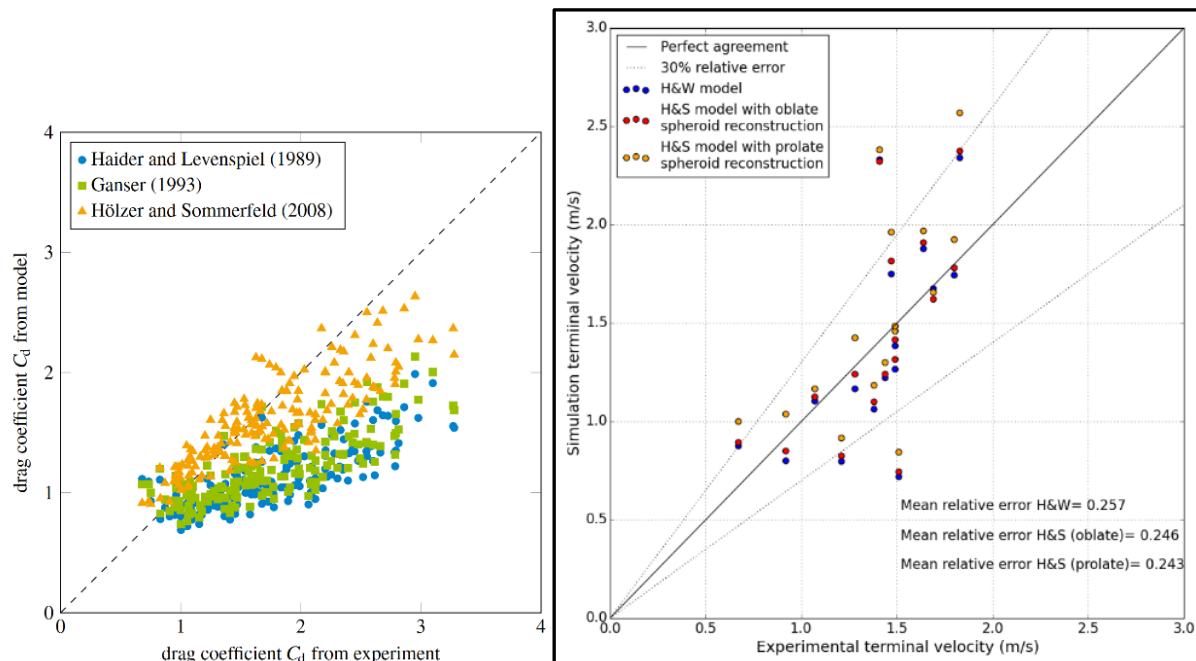


Figure 10: Drag models assessment. Left: drag coefficient comparison. Right: free-fall speed comparison.

4.1.2 Melting

4.1.2.1 Experimental study

To study a snowflake melting, TUDA has designed an apparatus, which is capable of producing snowflakes in a controlled environment in the laboratory. The sketch of the setup is shown in Figure 11 (left image). A short summary of the snowflakes formation is given here and further details are in [1]. After the ice crystals on the wires reach a sufficient size, the ice is shed by shortly heating the wires with an electric power supply. The shed ice crystals fall into a funnel where they aggregate and form a snowflake finally deposited on a movable plate. The shapes of these artificial snowflakes are shown in Figure 11 (middle image) in comparison with the natural snowflakes in Figure 11 (right).

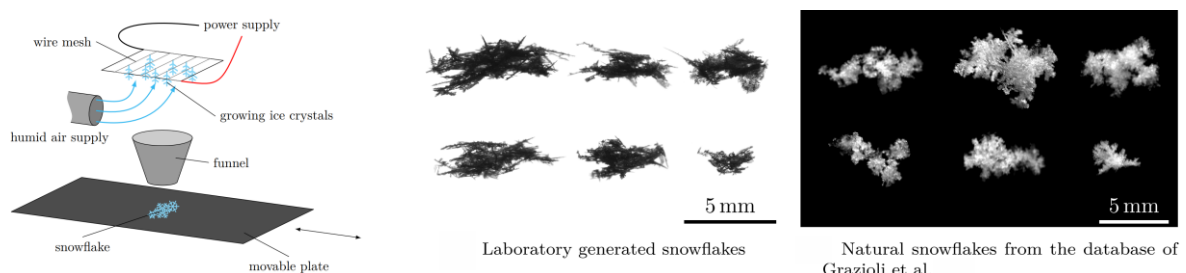


Figure 11: Left: snowflake production system consisting of a humid air supply, wires as nucleation sites and a funnel for aggregation. Middle: laboratory produced snowflakes [15]. Right: natural snowflakes [16]

The experimental setup developed by TUDA for the investigation of the melting of the generated snowflakes consists of the following main systems shown in Figure 12: an acoustic levitator to keep the snowflake in a fixed position, a warm air supply, including temperature and humidity sensors and an optical observation system. The entire setup is placed in a chest freezer in order to suppress melting prior to the start of the experiments.

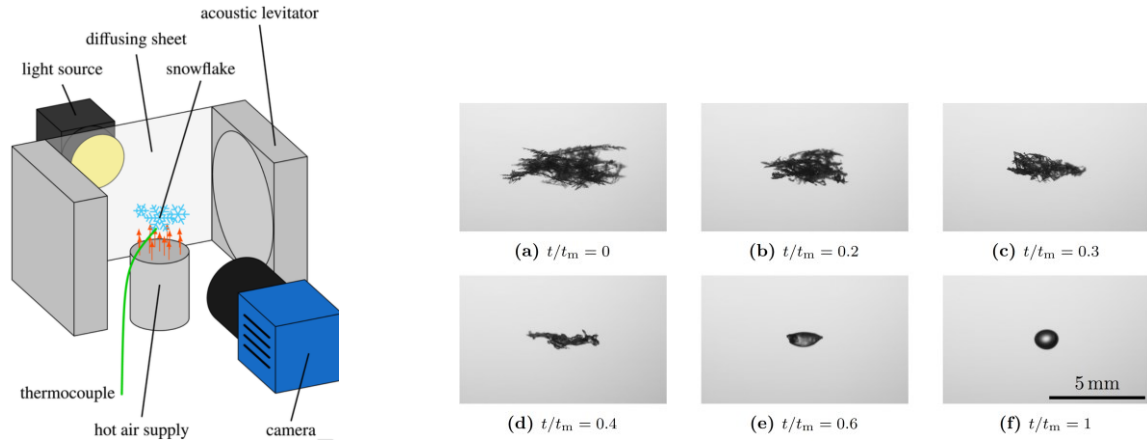


Figure 12: Melting process. Left: experimental setup for observation of melting of a laboratory produced snowflake. Right: melting process of an exemplary snowflake

Warm air is blown into a tube outside of the chest freezer. The air stream flows past a humidity sensor, which is located outside the freezer and not shown in Figure 12. The warm air is then directed towards the snowflake. The humidity of the warm air in the experimental runs ranges from dry air to fully saturated air. The air temperature at the snowflake is measured using a thermocouple with an exposed tip of 0.15 mm diameter, which results in a short response time. The thermocouple is located close to the snowflake in the free stream of warm air. The air temperature was varied from 4°C to 31.5°C. The velocity of the incoming flow ranged from 0.4 to 1.4 m/s.

The melting process is observed and recorded with a high-resolution camera and backlighting. A diffusing sheet is used to generate a uniform background. The camera records at a frame rate of 60Hz and at a resolution of 3840 pixel x 2160 pixel, corresponding to a field of view of 20.6mm 11.6mm.

One example of the melting process, captured by the camera, is shown in Figure 12 right using the melting time t_m . At the initial stage (stage I) of the particle melting, the liquid water is collected inside the porous particle due to the water imbibition driven mainly by the capillary forces. At some instant, the entire volume of the pores are filled by the liquid water and stage II begins when the drop is represented by the solid dendrites immersed in the liquid water at the temperature close to the melting point. The drop temperature starts to grow at stage III when the solid ice fraction is melted. It is obvious that the melting process has to be modelled differently for stages I, II and III.

4.1.2.2 Numerical models

Two main models have been considered by ONERA and TUDA, but this report only presents the ONERA model identified as the modified Nusselt and Sherwood numbers model (mNS model) [17], based on the Frössling's correlations [18]. The second model mostly assessed by TUDA corresponds to the Mitra's model [19].

For the ONERA model, the snow particle melting is described solving the following set of equations:

$$L_f(T_f) \frac{dm_{p,i}}{dt} = -\dot{m}_f L_f(T_f) = -\pi d_v \frac{Nu}{\Phi} k_a (T_a - T_p) + \dot{m}_{ev} L_v(T_f)$$

$$\frac{dm_p}{dt} = -\dot{m}_{ev} = -\pi d_v \frac{Sh}{\Phi} \rho_a D_{v,a} (y_{v,s}^{liq}(T_p, p_a) - y_{v,\infty})$$

with the Nusselt and Sherwood numbers (respectively Nu and Sh) are defined as:

$$Nu(\Phi, Re_p) = 2\sqrt{\Phi} + 0.55 Pr^{1/3} \Phi^{1/4} \sqrt{Re_p}$$

$$Sh(\Phi, Re_p) = 2\sqrt{\Phi} + 0.55 Sc^{1/3} \Phi^{1/4} \sqrt{Re_p}$$

where $m_{p,i}$ denotes the ice core mass of the particle and m_p the particle mass. The particle volume equivalent diameter is d_v , T_p the particle temperature, T_a the air temperature and T_f the melting

temperature ($T_p = T_f$ during melting). The latent heat of fusion is L_f , L_v the latent heat of evaporation, \dot{m}_f the melting rate and \dot{m}_{ev} the evaporation rate. Φ is the particle sphericity, k_a is the air conductivity, ρ_a is the air density, p_a the total air pressure and $D_{v,a}$ the vapor diffusivity. $y_{v,\infty}$ denotes the freestream steam mass fraction and $y_{v,s}^{liq}(T_p, p_a)$ is the saturated steam mass fraction at the surface of the particle computed above liquid water. Finally, Pr and Sc are respectively the Prandtl and Schmidt numbers. Two models have been derived to improve the initial melting model with different density and sphericity expressions and are called in the sequel “model 1” and “model 2”. It is preferable to use these models with an oblate spheroid reconstruction.

The model 1 writes:

$$d_V = \left[\frac{6}{\pi} \left(\frac{m_p - m_{p,i}}{\rho_w} + \frac{m_{p,i}}{\rho_{p,i}} \right) \right]^{1/3}$$

$$\rho_p = \frac{1}{2}(\rho_{p0} + \rho_w) + \frac{1}{2}(\rho_w - \rho_{p0}) \tanh \left(\frac{c_1}{1 - Y_w^{c_2}} - \frac{c_1}{Y_w^{c_2}} \right)$$

$$\Phi = \frac{1}{f_\Phi}, f_\Phi(Y_w) = \begin{cases} f_{\max} + (f_{\max} - f_{\Phi,0}) \tanh \left(\frac{c_1}{1 - Y_w^{c_2}} - \frac{c_1}{Y_w^{c_2}} \right), & Y_w \leq \frac{1}{2} \frac{1}{c_2} \\ f_{\max} - (f_{\max} - f_{\Phi,w}) \tanh \left(\frac{c_1}{1 - Y_w^{c_2}} - \frac{c_1}{Y_w^{c_2}} \right), & Y_w > \frac{1}{2} \frac{1}{c_2} \end{cases}$$

where c_1 and c_2 are constants chosen empirically such that $c_1 = 1.5$ and $c_2 = 3.5$, ρ_{p0} is the initial bulk density, $f_{\Phi,0} = \frac{1}{\Phi_0}$ is the dry value of f_Φ , $f_{\Phi,w} = \frac{1}{\Phi_1} = 1$ is the corresponding value at the liquid state, f_{\max} is set to 1.5, Φ_0 denotes the value of the particle sphericity at the beginning of the melting phase, $\rho_{p,i}$ and ρ_w are respectively the ice core and liquid water densities, $Y_w = 1 - \left(\frac{m_{p,i}}{m_p} \right)$ is the water mass fraction.

The model 2, presented in [17], uses the same relationship for d_V , but new bulk density and sphericity evolutions:

$$\rho_p = \frac{1}{2}(\rho_{p0} + \rho_w) + \frac{1}{2}(\rho_w - \rho_{p0}) \tanh \left(\frac{c_1}{1 - Y_w^{c_2}} - \frac{c_1}{Y_w^{c_2}} \right)$$

$$\Phi = (1 - Y_w)\Phi_0 + Y_w$$

where c_1 and c_2 are two parameters which were calibrated with TUDA and IAG melting experiments. Two expressions for these parameters have been proposed: one depending only on the initial bulk density ρ_{p0} and the second one depending on the initial bulk density ρ_{p0} and the initial circularity C_{l_0} .

The first proposal (P1 model 2) is expressed as:

$$c_1 = E_1 \left(\frac{\rho_{p0}}{\rho_s} \right)^{F_1}$$

$$c_2 = E_2 \left(\frac{\rho_{p0}}{\rho_s} \right)^{F_2}$$

with $E_1 = 0.307$; $E_2 = 0.183$; $F_1 = -0.247$; $F_2 = -0.801$ and $\rho_s = 917 \text{ kg/m}^3$ the ice core density.

The second proposal (P2 model 2) writes:

$$c_1 = E_1 \left(\frac{\rho_{p0}}{\rho_s} \cdot C_{l_0}^{G_1} \right)^{F_1}$$

$$c_2 = E_2 \left(\frac{\rho_{p0}}{\rho_s} \cdot C_{l_0}^{G_2} \right)^{F_2}$$

with $E_1 = 0.244$; $E_2 = 0.304$; $F_1 = -0.031$; $F_2 = -1.274$; $G_1 = 16.996$; $G_2 = -0.908$ and $\rho_s = 917 \text{ kg/m}^3$ the ice core density. More details on the model and its calibration are available in [13] and [17].

4.1.2.3 Preliminary assessment and down-selection – 2D numerical tools

At first, the Mitra's and mNS models have been assessed by comparison with some experimental data. Figure 13 presents the evolution of the reduced maximal diameter value with respect to the reduced time on the left and the comparison of the numerical melting duration vs. its experimental counterpart on the right. Both models agree quite well with the experimental data. It is also obvious that the mNS model significantly improves the prediction relatively to the widely used Mitra's model [19].

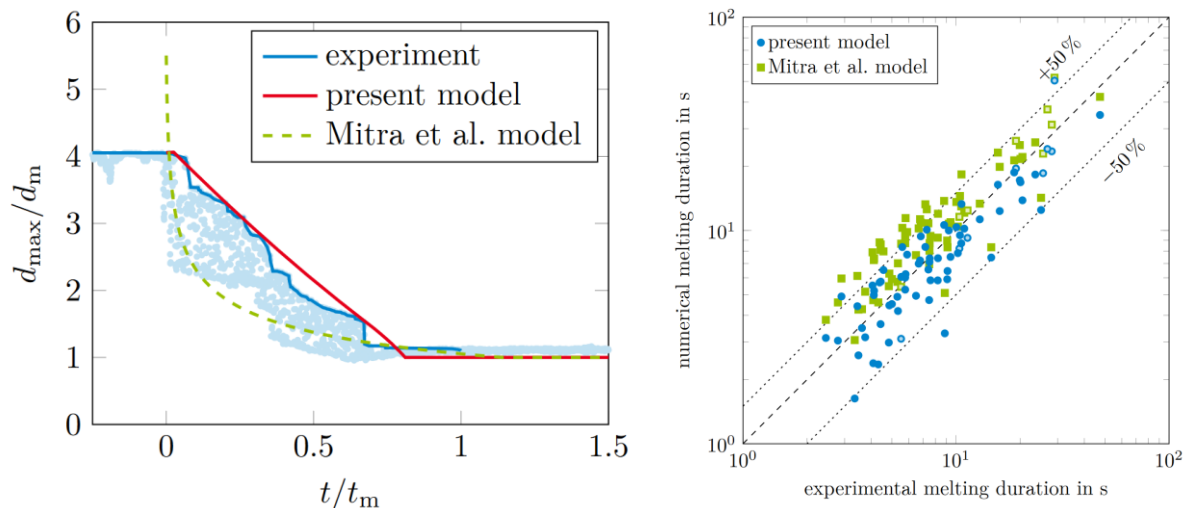


Figure 13: Melting process. Left: comparison of the reduced diameter vs. the reduced time. Right: comparison of the experimental and numerical melting times for both Mitra's and mNS models [15]

Next, further assessment has been performed by using ONERA's 2D icing suite IGLOO2D. The numerical melting times obtained by the different versions of the mNS model have been compared to the experimental melting time obtained by TUDA and IAG [17]. The operating conditions and the results of the experimental runs are presented in Annex 7.2. As seen in Figure 14, all of the models are able to reproduce the particle melting time with a relative accuracy of approximately 20%. Note that these results have been obtained with the oblate spheroid approximation. This is a rather good result considering the uncertainties on the experimental measurement and the difficulty to model properly this physical process. Moreover, it significantly improves the prediction relatively to the initial ONERA model or Mitra's model [19] which have a relative accuracy around 50% for the same cases.

As a conclusion, the mNS model (model 2 with option P1 or P2) using the oblate spheroid approximation has been down-selected as the best candidate for describing the melting process during the transport phase of a snowflake.

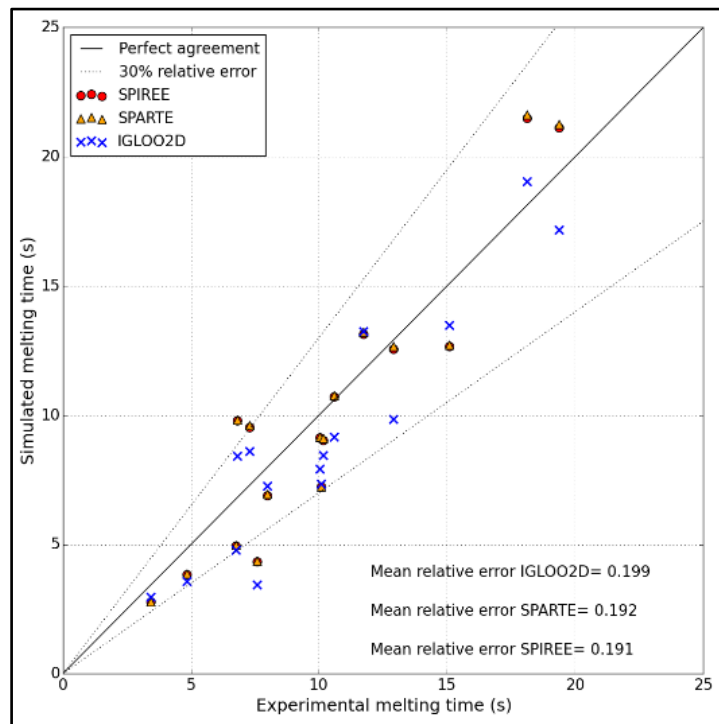


Figure 14: Comparison between experimental and numerical results for the snowflake melting time

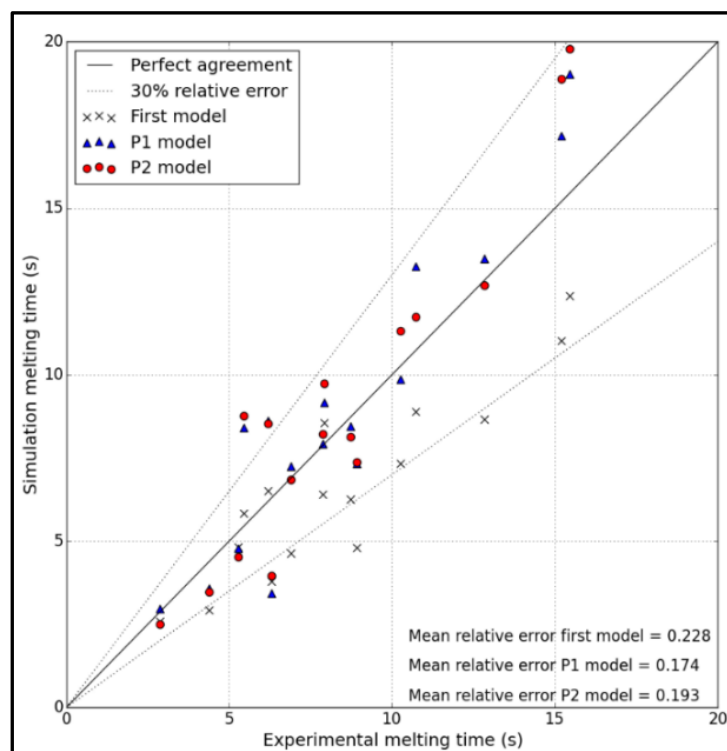


Figure 15: Comparison between experimental and numerical results for the snowflake melting time computed with IGLOO2D, CEDRE/SPIREE and CEDRE/SPARTE

4.2 Snowflake impact

4.2.1 Impact regime threshold

AIT and TUDA have performed impact experiments [1]. In TUDA case, snowflakes are held at rest using an acoustic levitator. The impact target is made of a polished aluminium disc having a diameter of 20 mm. This disc is attached to a tube made of carbon-fibre-reinforced polymer (CFRP) or brass which is guided inside a custom designed pneumatic cylinder. The pneumatic cylinder is attached to a time-controlled solenoid valve which is manually triggered at the same time as the image acquisition system. Impact velocities up to $\approx 30 \text{ ms}^{-1}$ can be achieved using a supply pressure of up to 16 bars. However, in the ICE-GENESIS experiments, only two impact velocities have been considered respectively around 1 m/s and around 19.2 m/s.

For recording of the impact process, a high-speed camera (Photron MC2.1) and a high luminosity LED backlight (Veritas Constellation 120E) in combination with a light diffusor plate was used. The framerate of the camera was set to 4000 fps and the spatial resolution of the images varied between $77.5 \text{ }\mu\text{m}/\text{pixel}$ and $107 \text{ }\mu\text{m}/\text{pixel}$ in the experiments. As the field of view of the camera is fixed in space and the target travels through it, the impact dynamics can only be observed as long as the target is visible in the field of view. Therefore, in the experiments with high impact velocities, a wider field of view was used to capture as much as possible of the impact dynamics, resulting in a coarser resolution. An example image sequence of a snowflake impact is shown in Figure 16 for a velocity close to 1 m/s. For the higher velocity of impact, the fragments are close to being spherical and their size is in the order of the spatial resolution (approximately $100 \text{ }\mu\text{m}$).

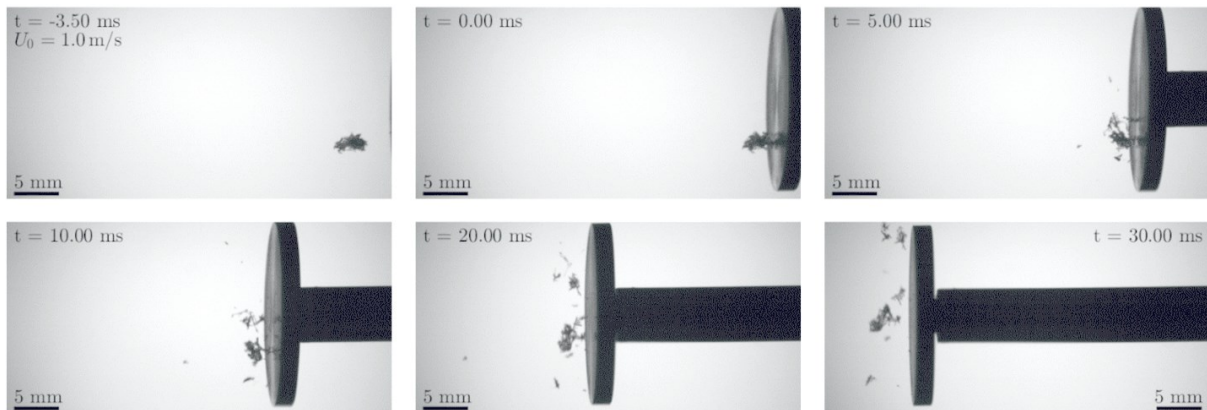


Figure 16: Sequence of aluminum target impact onto a levitated snowflake at 1 m/s

In Figure 17, the parameter $\xi = U_n D_{\min}^{2/3} / \beta$ is plotted against the length scale ratio D_{\min} / D_{\max} for the experimental data for snowflakes, using the impact velocity in normal direction to the target, U_n . In the definition of ξ for snowflakes, the smallest length scale D_{\min} is used because it is hypothesized to be the relevant length scale for the breakup of the snowflake structure.

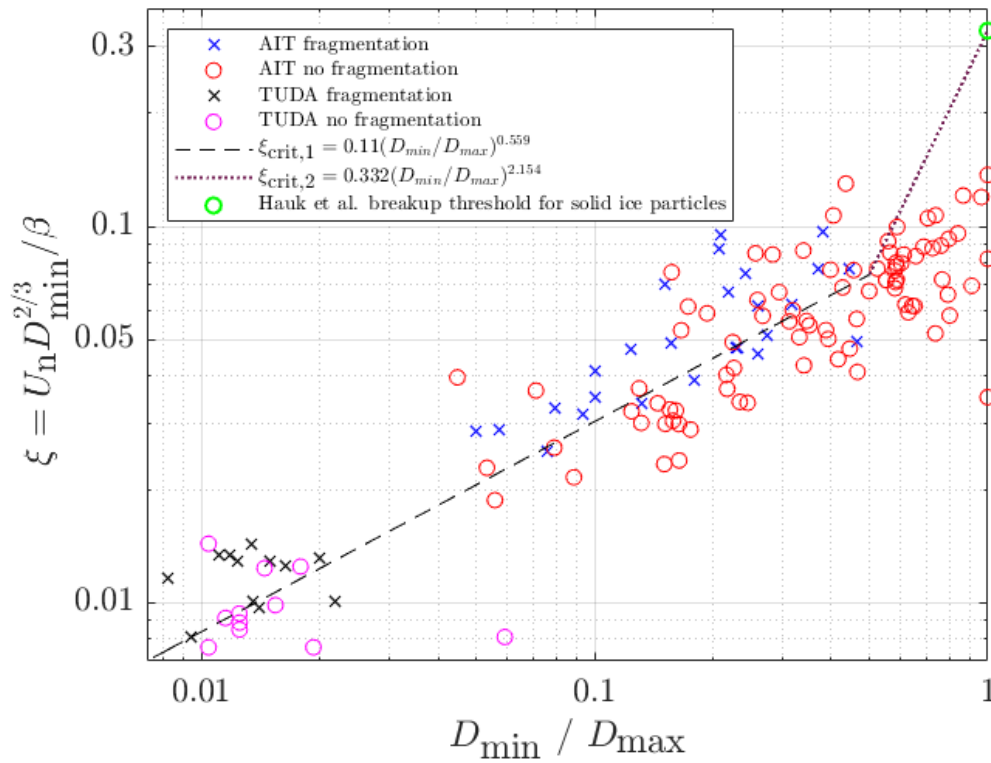


Figure 17: Dimensionless parameter $\xi = U_n D_{\min}^{2/3} / \beta$ vs. the length scale ratio D_{\min} / D_{\max} (AIT data in red and blue markers; TUDA data in black and magenta markers; solid ice particles data in green Hauk et al. [6])

As expected, the breakup threshold value of ξ for smaller values of D_{\min} / D_{\max} decreases because the snowflakes become more fragile. For smaller values of $0.008 < D_{\min} / D_{\max} < 0.5$, experiments for both fragmentation and no fragmentation exist and the breakup threshold appears to be a linear function of D_{\min} / D_{\max} in this double logarithmic plot. Therefore, a power law can be fitted to the breakup threshold in this range, shown as a black dashed line:

$$\xi_{\text{crit},1} = 0.110 \left(\frac{D_{\min}}{D_{\max}} \right)^{0.559} \quad \text{for } [0.008 < D_{\min} / D_{\max} < 0.5]$$

In the range $0.5 < D_{\min} / D_{\max} < 1$, no experiments for fragmentation exist and as a first approximation, another power law is used, connecting the point $\left[\frac{D_{\min}}{D_{\max}} = 0.5, \xi_{\text{crit},1} \left(\frac{D_{\min}}{D_{\max}} = 0.5 \right) \right]$ and the threshold of Hauk $\left[\frac{D_{\min}}{D_{\max}} = 1, \xi_{\text{crit},0} = 0.3315 \right]$ obtained for solid ice particles as shown as dotted line in Figure 17:

$$\xi_{\text{crit},2} = 0.3315 \left(\frac{D_{\min}}{D_{\max}} \right)^{2.154} \quad \text{for } [0.5 < D_{\min} / D_{\max} < 1]$$

In conclusion, a model for the breakup threshold is formulated using the length scale of the smallest structures of the snowflake, D_{\min} , which is assumed to determine the snowflake strength. Using the available experimental data from TUDA and AIT, the breakup threshold model from Hauk et al. [6] is adapted introducing the length scale ratio D_{\min} / D_{\max} . Two empirical fits are used to define the breakup threshold for snowflakes. An advantage of the model formulation is that for the limit of $D_{\min} / D_{\max} \rightarrow 1$, the breakup threshold is equal to the formulation of Hauk et al. for solid ice particles.

4.2.2 Shattering

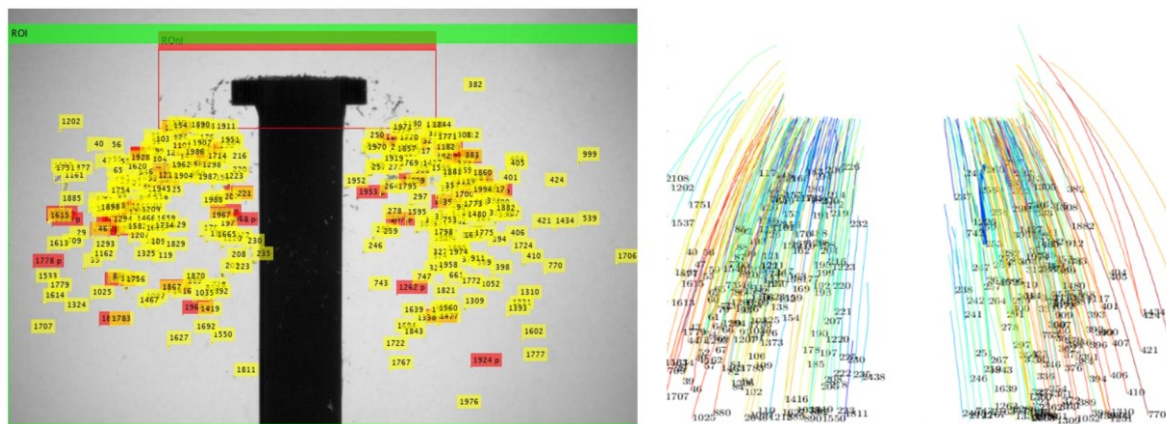


Figure 18: Example of the post-processing procedure of one snowflake impact video. Left: tracked objects with their red and yellow ID labels. Right: visualization of the individual particle trajectories

The individual fragment sizes are analyzed using in-house codes written in the commercial software package Matlab taking into account 19 observed impacts. It uses an in-house developed Kalman multi object tracking algorithm to track each individual ice fragment after the snowflake impact. This way, as many as possible fragments are captured, compared to using a single video frame for the analysis, since some fragments leave the field of view of the camera while others are still overlapping each other and are not separable in the image processing. In Figure 18, an example of the post-processing routine is shown. On the left image, one frame of the multi object tracking routine is shown. The large green box indicates the user-defined region of interest and the red box corresponds to the user-defined region of non-interest (RONI) which is excluded for the analysis. In the RONI, the fragments are too close together and overlapping. In the algorithm, in each subsequent video frame, each fragment is assigned to a track having an individual ID. The track IDs can be seen in the left image of Figure 18 as red and yellow label boxes. In the right image in Figure 18, the tracking result is shown where all fragment trajectories are visualized by different colored lines. In a post-processing routine, the found tracks are manually checked for plausibility.

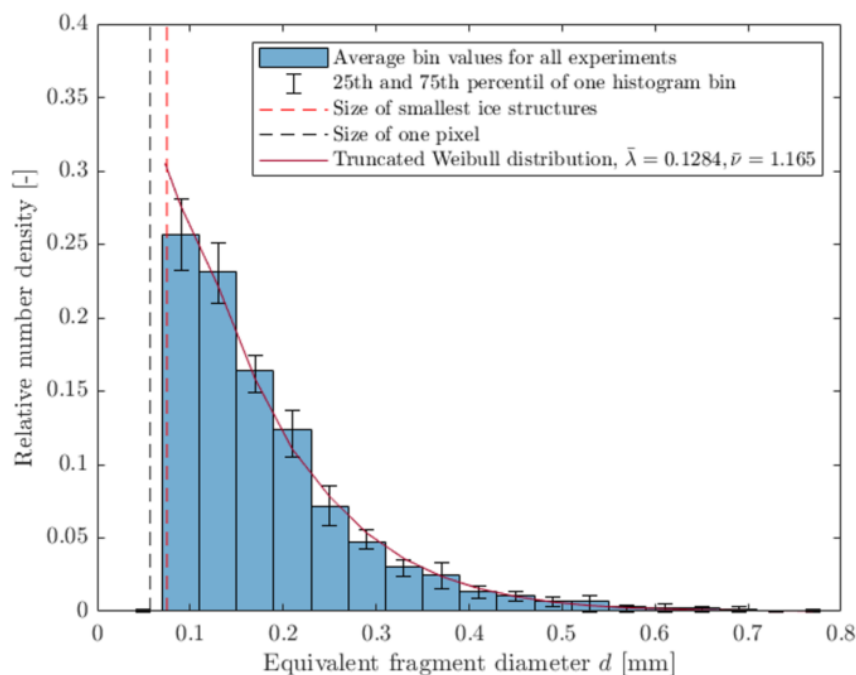


Figure 19: Averaged number density histogram of the generated fragments after snowflake impact

The data for the probability density of the fragment sizes after snowflake breakup are modelled using a left truncated Weibull distribution density function,

$$f(d) = \frac{\nu}{\lambda} * \left(\frac{d}{\lambda}\right)^{\nu-1} * \exp\left(-\left(\frac{d}{\lambda}\right)^{\nu}\right) \quad \text{if } d > 0.073 \text{ mm},$$

where λ and ν are free parameters. A left truncated distribution is used since in the high-speed videos it was observed that the snowflake did not break apart into fragments smaller than the smallest ice structures. Hence, for the truncation value for the distribution, the measured size of the smallest structures of $d = 0.073$ mm is used. As it can be seen, the proposed left truncated Weibull distribution function fits the experimental data very well. This procedure is repeated for every experiment. The resulting free parameters λ and ν are averaged resulting in:

$$\bar{\lambda} = 0.1284, \bar{\nu} = 1.165$$

The truncated Weibull distribution with the averaged parameters $\bar{\lambda}$ and $\bar{\nu}$ (solid red line) is compared in Figure 19 to the average bin values of the relative number density distribution of all experiments combined. The dashed vertical line in black corresponds to the physical size of one pixel in the recorded images and the dashed vertical line in red indicates the average value of the smallest ice structures. The vertical error bars indicate the 25th and 75th percentile of each histogram bin.

4.2.3 Accretion

4.2.3.1 Numerical models

To compute the ice accretion for droplet impacts, the well-known Messinger balance is usually solved and an extension of this formulation has been proposed by Wright [20] and Villedieu [21] to account for the impact of solid crystals. Such a balance makes appear, in particular, the particle deposited mass rate \dot{m}_{dep} and erosion mass rate \dot{m}_{er} .

The particle deposited mass rate \dot{m}_{dep} derives from the impinging mass rate \dot{m}_{imp} through the sticking efficiency ϵ_s following the equation:

$$\dot{m}_{dep} = \epsilon_s \dot{m}_{imp}$$

The sticking efficiency coefficient ϵ_s is determined with the empirical model developed in the framework of the European HAIC project [22] as:

$$\epsilon_s = F(\eta_m) \quad \text{with } F(\eta_m) = (K_c - 2)\eta_m^3 + (3 - 2K_c)\eta_m^2 + K_c\eta_m$$

where η_m represents the melting fraction of the particle and K_c is a constant calibrated and set to 2.5.

Concerning the erosion mass rate \dot{m}_{er} , the HAIC model [22] has been used for the snow conditions and writes as:

$$\dot{m}_{er} = \min[\dot{m}_{acc,s} + \dot{m}_{Mess}; \min(1, \epsilon_{er}) \cdot \dot{m}_{imp}]$$

where \dot{m}_{imp} is the impinging mass rate and $\dot{m}_{acc,s}$ and \dot{m}_{Mess} represent respectively the amounts of solid and liquid water available on the wall. The erosion efficiency ϵ_{er} is determined with the following empirical model:

$$\epsilon_{er} = E_0 \left(\frac{V_{t,imp}}{V_0} \right) \cdot \frac{y_{l0}}{y_{l0} - \min(y_l, y_{l0})} \cdot [1 + (l_0 \kappa)^2]$$

where $V_{t,imp}$ denotes the mean tangential velocity of the impinging particles and y_l is the wall liquid mass fraction defined by:

$$y_l = \frac{\dot{m}_{acc,l}}{\dot{m}_{acc,l} + \dot{m}_{acc,s}}$$

where κ is the local curvature of the ice layer surface. The parameters E_0 , V_0 , y_{l0} and l_0 are empirical constants estimated by Baumert [23]. The first three ones are set respectively to 0.314466, 84.5 and 0.6. The l_0 parameter depends on the airfoil chord c as follows : $l_0 = 0.015 * c$.

4.2.3.2 Initial study on the CSTB and RTA database

During this project, experiments on snow accretion have been performed in the CSTB climatic wind tunnel [13]. The injection system used during the tests produces partially melted ice balls (artificial snow particles) which are not representative of snow aggregates. Four temperatures and different Liquid Water Ratios (LWR) have been tested for two air velocities: 46 m/s considered as a typical helicopter speed and 94 m/s to accentuate the erosion effects. All the operating conditions of the experimental runs are gathered in Table 1.

Exp.	M_∞	T_∞ (°C)	RH_∞	MMD (μm)	TWC (g/m^3)	LWR	Duration (s)
Run401	0.139	-1.3	1	96	4.12	0.43	600
Run403	0.140	-3.2	0.97	96	5.08	0.33	600
Run405	0.140	-5.2	0.95	96	3.22	0.12	600
Run407	0.141	-7.2	0.94	96	3.21	0.15	600
Run901	0.284	-1.3	1	96	3.99	0.55	600
Run903	0.285	-3.2	0.97	96	3.73	0.36	600
Run905	0.287	-5.2	0.95	96	3.04	0.22	600
Run907	0.288	-7.2	0.94	96	2.93	0.23	600

Table 1: Experimental data of CSTB ice accretion experiment with snow conditions

Preliminary numerical simulations of the CSTB cases have been performed with the ONERA's 2D icing suite, IGLOO2D [24], using the HS drag model, and the HAIC sticking and erosion models previously described. A multistep approach with a time-step of 60 seconds has been adopted. Figure 20 and Figure 21 present the numerical results obtained for Run405 and Run905 compared to the experimental ice shapes. Both figures show clearly that some discrepancies exist between experimental and numerical ice accretions. These comparisons show that the erosion and sticking models do not really capture the physics of snow accretion. The other cases are provided in the Annex 7.3.

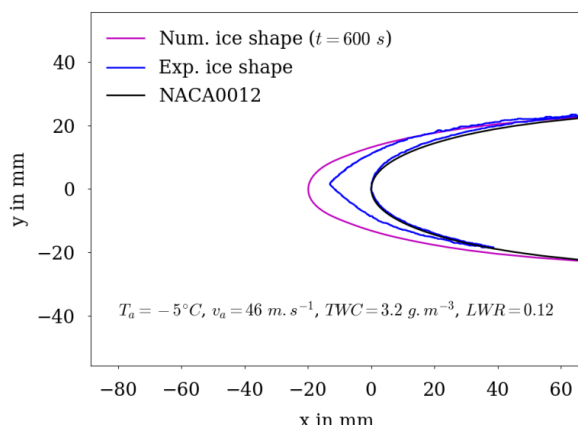


Figure 20: Numerical ice shape for CSTB-Run405

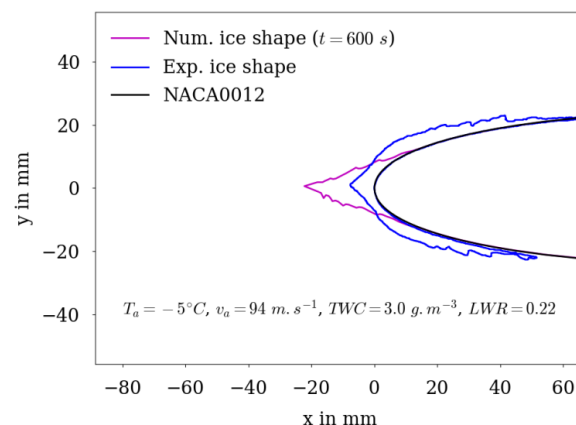


Figure 21: Numerical ice shape for CSTB-Run905

The second dataset used is the one from the RTA experiment performed in the framework of ICE-GENESIS project. It consisted in measuring the ice accretion on an unheated NACA0012 under snow conditions. The particles were much more representative of real snowflakes than in the CSTB experiment with a Median Mass Diameter (MMD) around 600-800 μm . The operating conditions are presented in Table 2.

Exp	V_∞ (m/s)	T_∞ (°C)	MMD (μm)	TWC (g/m^3)	LWR	Density (kg/m^3)	Estimated duration (s)
TP07	40	-3	617	0.33	0.15	160	600
TP08	40	-3	699	0.49	0.3	280	900
TP09	40	-3	745	0.71	0.45	480	780
TP14	40	-3	702	0.43	0.3	280	840
TP15	40	-3	764	0.61	0.45	480	720
TP19	40	-3	697	0.44	0.3	280	2160
TP20	40	-3	741	0.58	0.45	480	2040
TP21	40	-1	790	0.64	0.45	480	900
TP22	40	-1	748	0.41	0.3	280	780

Table 2: Experimental data of RTA ice accretion tests with snow conditions

Simulations of these cases have been performed to evaluate the behaviour of the current HAIC sticking and erosion models, comparing the numerical ice shapes to the experimental ones. These simulations have been done with IGLOO2D in the same way as previously presented for the CSTB cases, using the HS drag model, and the HAIC sticking and erosion models. A multistep approach has also been adopted for this study with a time-step of 60 seconds.

Figure 22 and Figure 23 present the comparisons of both numerical and experimental ice shapes for cases TP08 and TP09. The other comparisons are available in the Annex 7.3. The IGLOO2D simulations tend to overestimate the ice accretion compared to RTA experiment.

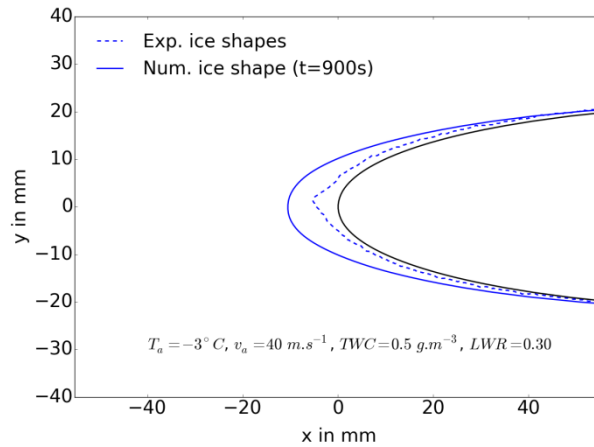


Figure 22: Ice shape comparison for RTA-TP08

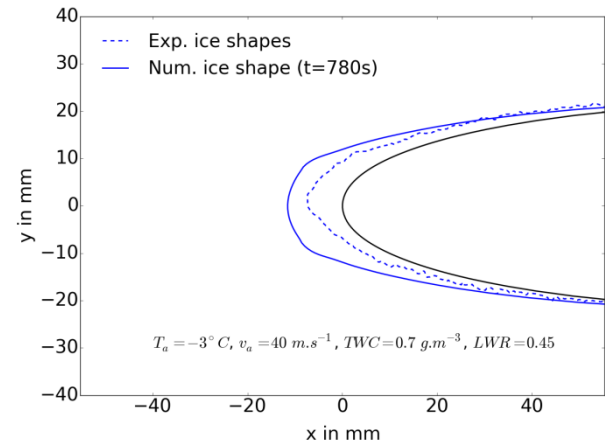


Figure 23: Ice shape comparison for RTA-TP09

In the sequel, two investigations have been performed to improve the comparisons. The first one aims at assessing the sensitivity of the numerical results to the measurement uncertainties and the second one at improving the behaviour of the current HAIC models by modifying their parameters through an optimization method.

4.2.3.3 Sensitivity study to the measurement uncertainties

A study on the sensitivity of the final accretion shapes as a function of the TWC and LWR has been done on the CSTB database. Taking into account the experience of the HWD probe suppliers who estimate a measurement uncertainty of less than or equal to 20%, we have varied the values of TWC and LWR between -20 % to +20 % for the eight runs. The scalar δ of interest used for this study, illustrated in Figure 24, is defined as the difference (in absolute value) between the experimental and numerical maximal accretion length at the leading edge.

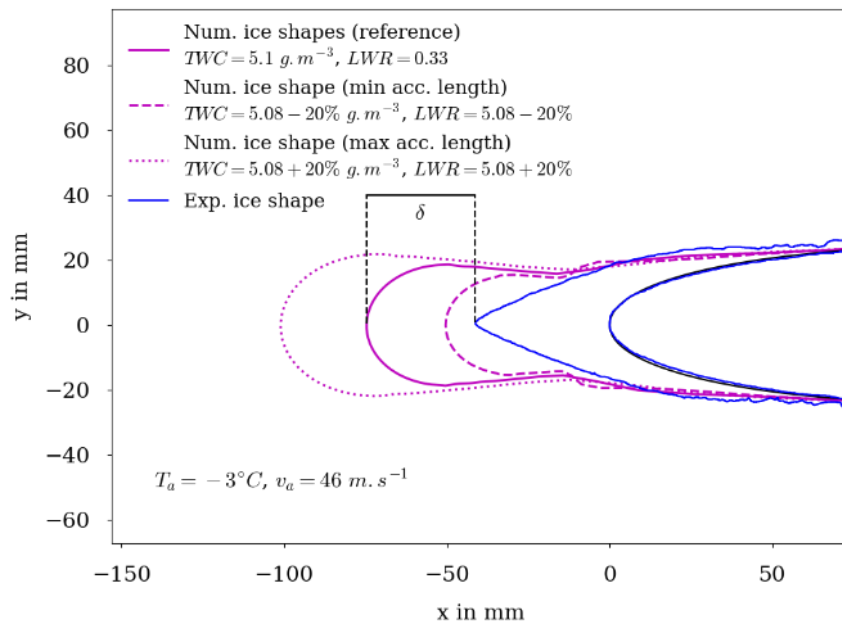


Figure 24: Sensitivity numerical results for Run403

The objective was to determine if there was a bias of estimation of the probes that would improve the numerical results. It is important to specify that this study did not aim at taking, if necessary, a correction on the values indicated by the probes. This would have been possible if we had had an absolute confidence in the empirical models involved in the accretion computation, but it is not the case.

In order to find a possible bias, the mean deviation $\tilde{\delta}$ is defined as follows:

$$\tilde{\delta}_{i,j} = \frac{1}{N} \sum_{k=1}^{k=N} \left(\frac{(\delta_{i,j})_k - \min_{i,j}(\delta_{i,j})_k}{\max_{i,j}(\delta_{i,j})_k - \min_{i,j}(\delta_{i,j})_k} \right),$$

where $N = 8$ is the number of experimental runs considered. The indexes i and j refer to the uncertainties introduced respectively on the TWC and LWR values.

Figure 25 summarizes the results of this sensitivity study in the form of an image composed of 121 pixels. A color is assigned to each pixel going from light green for the best deviation from the standard of the whole base ($\tilde{\delta}_{i,j} = 0$) to dark blue for the worst ($\tilde{\delta}_{i,j} = 1$). The iso-error lines of $\tilde{\delta}_{i,j}$ are represented by the black solid lines. It can be deduced that the probes may have a tendency to overestimate the TWC and LWR measurements and that the minimal deviation is obtained for -20% of TWC and -20% of LWR.

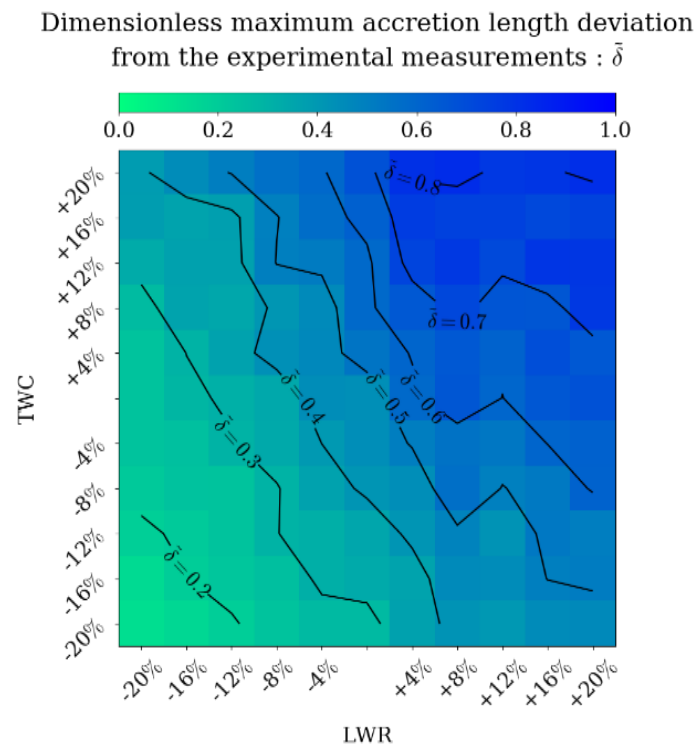


Figure 25: Numerical sensitivity results

The final ice shapes computed using these optimal values (-20% of TWC and -20% of LWR) are displayed in Figure 26 and Figure 27 for Run 405 and Run 905 (see Annex 7.4 for the other runs). The “optimal inputs” ice shape is represented by a solid green line, the reference ice shape obtained using the TWC and LWC experimental measures by a solid purple line and the experimental ice shape by a solid blue line. The decrease in the TWC and LWR values leads to an ice accretion reduction, improving the numerical ice shape which becomes closer from the experimental one. The uncertainties on the measurements could partly justify the discrepancies observed between the numerical and experimental results. However, it does not seem to be the only factor and an analysis of the sticking and erosion models has been conducted to see if further improvements were possible.

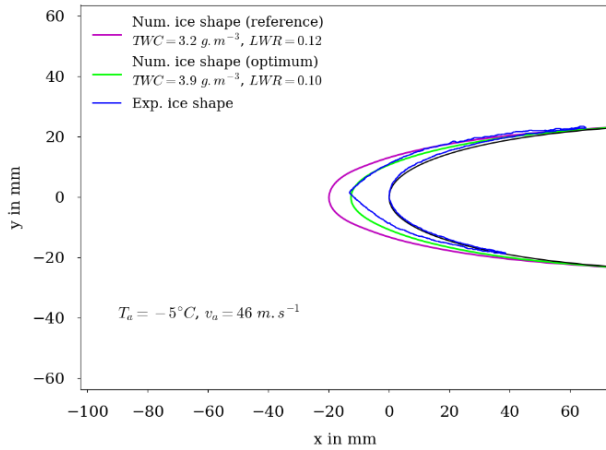


Figure 26: Sensitivity to the measurement uncertainties for CSTB-Run405

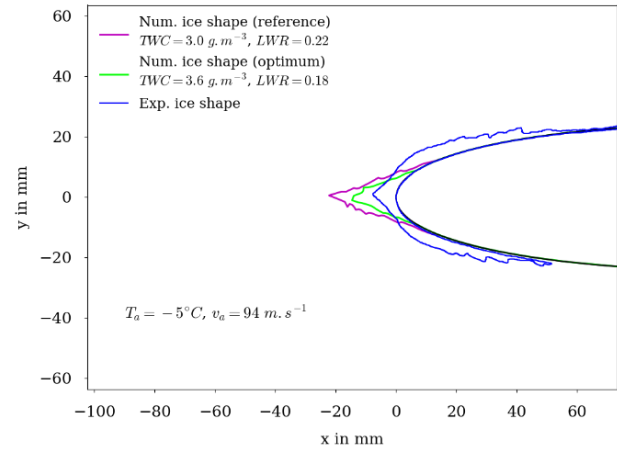


Figure 27: Sensitivity to the measurement uncertainties for CSTB-Run905

4.2.3.4 Optimization study on the HAIC models

As the HAIC models for sticking efficiency and erosion have been calibrated for ice crystals conditions, one can question the possibility to improve the numerical results by recalibrating some of their coefficients for snow conditions. As a matter of fact, the sticking efficiency coefficient K_c from the sticking efficiency model, the erosion coefficient E_0 and wall liquid mass fraction threshold y_{l0} from the erosion model have been selected for this study. The recalibration is based on an optimization process.

This optimization process consists in fitting the set of the three coefficients evocated previously (K_c , E_0 , y_{l0}) to obtain the best agreement possible between the numerical and experimental ice shapes through a severity function. Considering that the experimental ice shapes are defined by a set of N points of coordinates $(x_{exp,i}, y_{exp,i})$ with $x_{exp,i} \leq 0$ (the points downstream of the leading edge are not accounted for) and that the function $f_{(K_c, E_0, y_{l0})}(y)$ is the interpolating linear function of the numerical ice shape computed using IGLOO2D with the coefficients K_c, E_0 and y_{l0} , the severity function to minimize for one test case is:

$$\min_{K_c, E_0, y_{l0}} \sqrt{\frac{\sum_{i=1}^{i=N} (x_{exp,i} - f_{(K_c, E_0, y_{l0})}(y_{exp,i}))^2}{N}}$$

A Trust Region Reflective algorithm has been used in order to solve this optimization problem. It is generally a robust method which is similar to a gradient descent algorithm, but with a slightly better convergence. Note that a set of optimal coefficients can be defined for each experimental ice shape and we have also calculated a global set of optimal coefficients on several cases by considering the arithmetic mean of the all of the optimal coefficients.

Concerning the first possibility – a set of optimal coefficients calculated for each case separately –, the algorithm has been employed for both RTA and CSTB database. Figure 28, Figure 29, Figure 30 and Figure 31 show the best results obtained with each specific set of optimal coefficients related to each case (red line) for CSTB-Run403 and CSTB-Run903, and RTA-TP08 and RTA-TP09 cases. The experimental ice shape are plotted in blue dashed line. For the relatively low velocity cases, the numerical “optimal” ice shapes fit rather well the experimental ice shape while, for the relatively high velocity case, the results are less convincing. More precisely, the optimal solutions reproduce quite nicely the ice thickness at the leading edge, but fail to predict the accretion limits. Moreover, the result obtained for CSTB-Run 903 performs very poorly. This case has not been retained in the sequel.

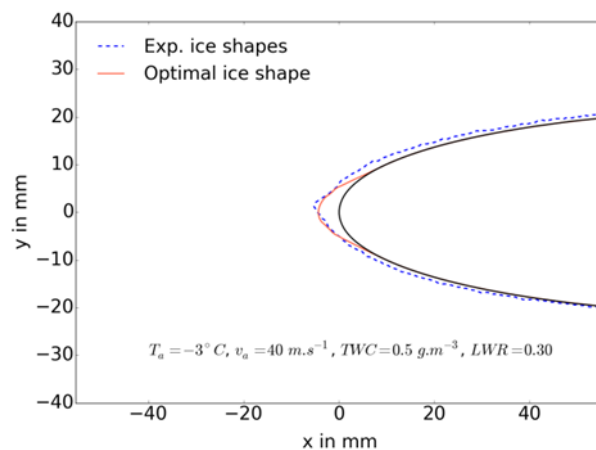


Figure 28: Ice shape comparison using the optimal coefficients for CSTB-Run 403

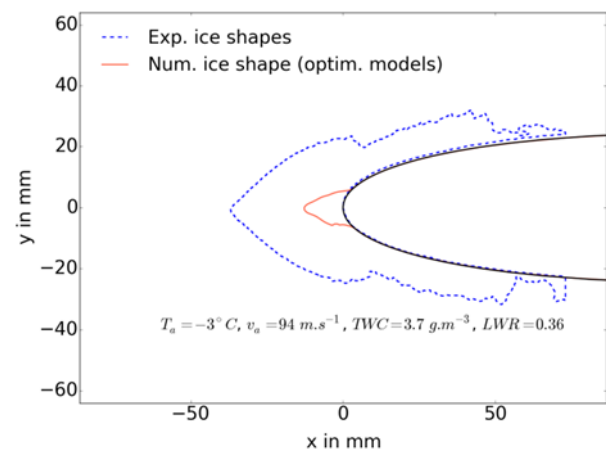


Figure 29: Ice shape comparison using the optimal coefficients for CSTB-Run903

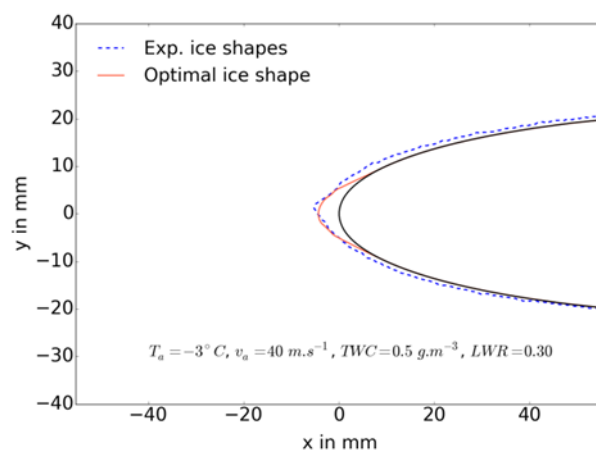


Figure 30: Ice shape comparison using the optimal coefficients for RTA-TP08

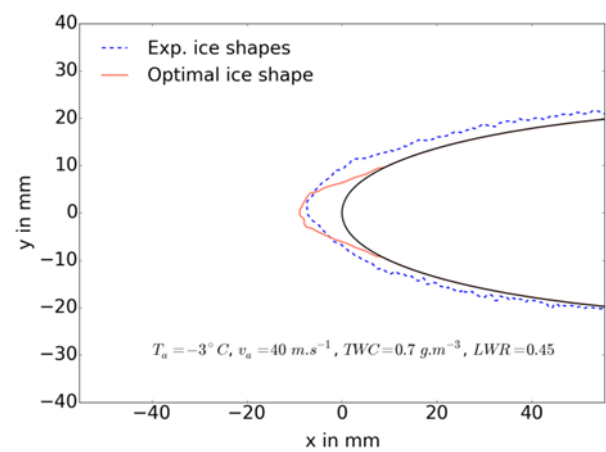


Figure 31: Ice shape comparison using the optimal coefficients for RTA-TP09

The next step consisted in calculating a set of optimal coefficients as the arithmetic mean of the coefficients specific to each case. Such a choice leads to the following values: 1.28 for the sticking coefficient K_c , 0.65 for the erosion coefficient E_0 and 0.6 for the liquid fraction threshold y_{l0} . Additional simulations have been computed with these mean values. The ice thicknesses (dashed line) plotted versus time are compared to the experimental results (symbols + linear fit) as well as those obtained with the initial HAIC sticking and erosion models (solid line) for the RTA cases TP07, TP08 and TP09 in Figure 32. The tendencies are rather good since the ice thicknesses or, equivalently, the ice accretion rates are reduced, but the discrepancies are still quite important in comparison with the experimental measurements. The corresponding ice shapes obtained are plotted in Annex 7.5. Figure 33 and Figure 34 show the final ice shape computed using these optimal coefficients for the CSTB Run403 and Run905 cases, compared to the initial ice shape obtained and the experimental one. An improvement of the results is also observed for the CSTB cases, but there are still some discrepancies with underestimations of the ice accretion.

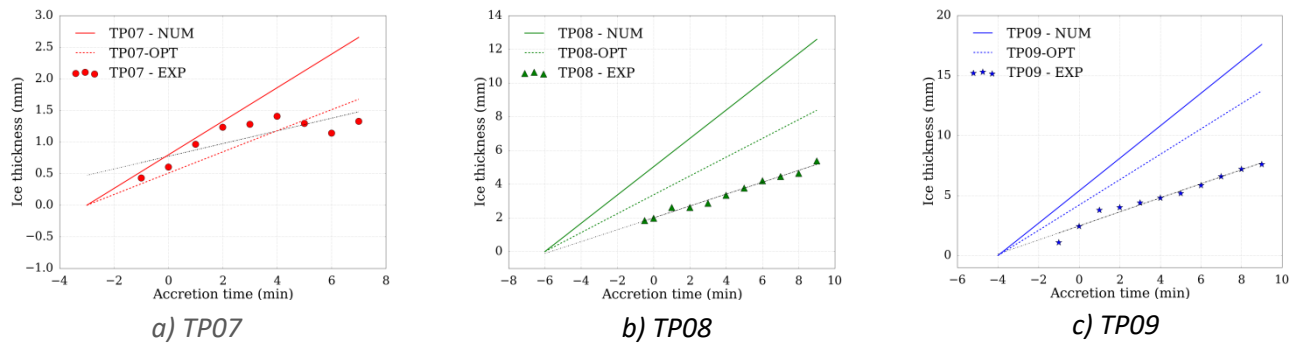


Figure 32: Numerical ice thickness over the time obtained using the optimised HAIC models compared to the experiments

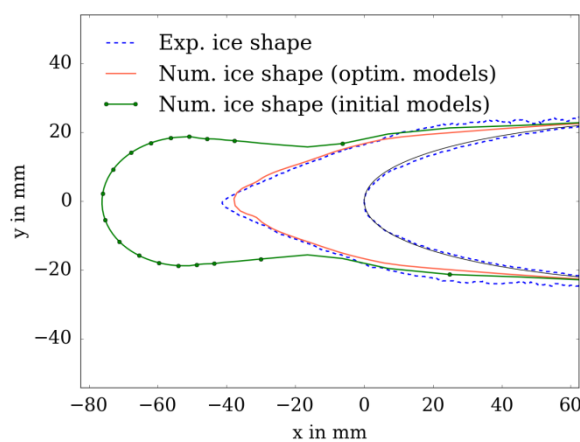


Figure 33: Ice shape comparison using the mean optimal coefficients for Run403

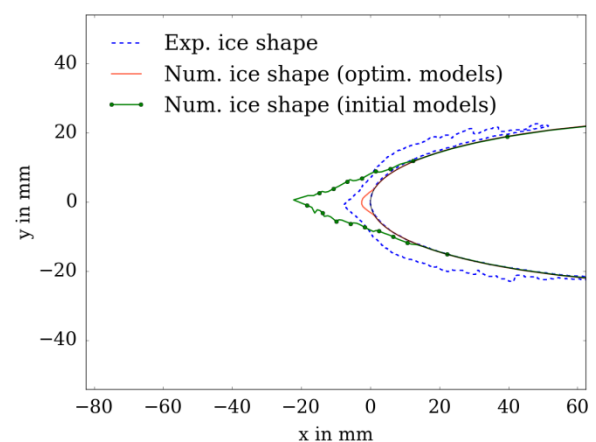


Figure 34: Ice shape comparison using the mean optimal for Run905

A global optimization has also been tested. Instead of optimizing the sticking and erosion coefficients for each case and computing their arithmetical mean, the global optimization aims to directly find the set of coefficients which minimizes the global sum of the errors computed between all the corresponding numerical and experimental ice shapes from cases of both CSTB and RTA database. Similar coefficients as for the previous optimization has been obtained with this global optimization, leading to some improvements in the comparison with experimental data. However, discrepancies are still present.

As a conclusion, it seems necessary to keep working on this topic either by defining a better optimization or by improving the modelling itself. Concerning the first point, note that the optimization process may conduct to inappropriate values for the coefficients, not respecting the expected physical behaviour of the sticking or erosion phenomena.

POLIMI has performed some activities on the uncertainty quantification by realizing numerical simulations. Further details can be found in [25], [26] and [27]. Such an approach needs to be considered for the numerical computation of ice accretion in the future.

5 Snow numerical capability in the 3D numerical tools

The snow models developed in Task D10.3, namely the HS drag model and the mNS melting model using the oblate spheroid geometrical description, have been integrated by AIT in ANSYS CFX and by ONERA in its in-house CEDRE computational platform. For ANSYS CFX, the models are present in the Lagrangian particle tracking solver. For CEDRE, the models are available in the SPARTE Lagrangian solver or its Eulerian counterpart SPIREE.

As a preliminary step, the free-fall and melting time cases have been reproduced using the 3D numerical tools and compared to the 2D reference solutions. For the drag part, the HS model has been implemented into the SPIREE and SPARTE solvers and their implementation assessed based on TUDA free fall experiments. The comparison of the different terminal velocities obtained for the three codes using the HS model with oblate spheroid reconstruction is displayed in Figure 35 left. The three solvers provide very comparable terminal velocities for each case and a good agreement with the experimental data. For the melting part, Figure 35 right shows the numerical results obtained with SPIREE, SPARTE and IGLOO2D using the mNS model 2 -P2 model compared to the experimental data. The numerical results obtained by IGLOO2D, SPIREE and SPARTE are in quite good agreement with rather similar melting times. However, some discrepancies exist between the three solvers due to differences of implementation/models related to the modelling of the thermo-physical properties.

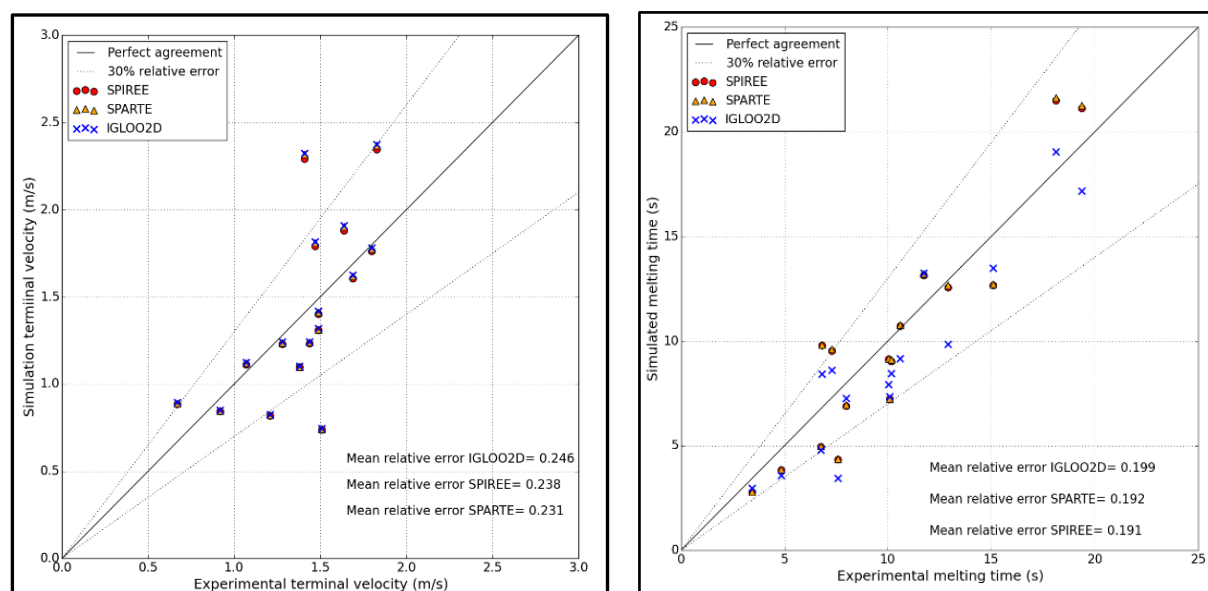


Figure 35: Left: comparison of the free fall velocities. Right: comparisons of melting times 2D solver vs. 3D solvers

In a second time, additional test cases have been performed by ONERA and they correspond to 2D extruded cases taken from the RTA database (TP08, TP09) and the operating conditions have been already reported in Table 2. The particle trajectories have been computed with both SPIREE and SPARTE solvers, using the HS drag model, the mNS thermal model with the P1 mass density evolution model, and the sticking and erosion models from HAIC project implemented in the accretion solver MESSINGER3D. The reference solution is provided by the ONERA solver IGLOO2D, using the same models.

As observed in Figure 36, IGLOO2D, SPIREE and SPARTE give a similar collection efficiency despite a small decrease of the latter at the stagnation point for SPARTE and, to a lesser degree, for SPIREE. Concerning the ice accretion computation, the same models and parameters have been used with IGLOO2D or IGLOO3D. The final ice shape obtained with both ice accretion solvers, compared in Figure 37, are in a very good agreement. The only difference takes place at the stagnation region due to the

collection efficiency discrepancy already mentioned. The second case TP09 provide similar results. These results validate the implementation of the different models in the ONERA's 3D icing suite.

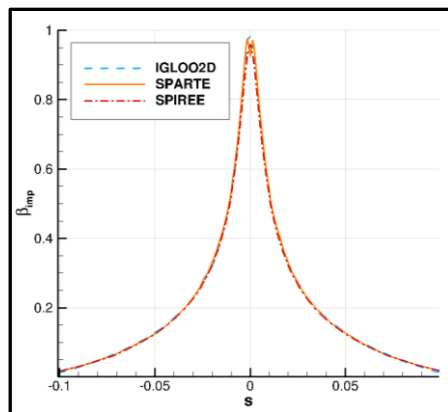


Figure 36: Impacting collection efficiency – TP08

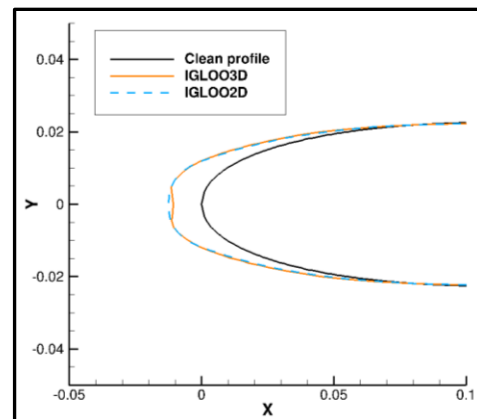


Figure 37: Ice shapes - TP08

6 Conclusions

As mentioned in the Introduction, many phenomena are of concern for in-flight snow icing and some of them have been addressed during ICE-GENESIS. At first, particle drag and thermal aspects of particle melting have been deeply studied, leading to two adapted models, respectively the Hölzer-Sommerfeld model and the mNS model. It is recommended to use these models with a geometric description of the snowflake based on the oblate spheroid approximation while the convex hull is another relevant choice, but may need some further developments. Besides, the 2D geometry descriptors are quite representative of a snowflake geometry, an important feature since most of the visual data correspond to images, i.e. 2D data. These two models are now available –and assessed- in both 2D and 3D numerical tools of two of the partners of the WP10. A TRL4 Review was carried out successfully in 2022.

Concerning the accretion part, two models have been proposed to describe the snowflake impact phenomenon and, more specifically, the break-up threshold and the particle shattering. They constitute a first promising step towards a more general modelling, considering larger impact velocities or more different types of snow particles. Another activity conducted during ICE-GENESIS has dealt with the sticking and erosion phenomena. From the very beginning of the project, it has been decided to use the Ice crystals models from the HAIC project, in order to assess their use for snow particles. Two numerical studies have been performed to evaluate either the influence of some measurement uncertainties on the numerical computations, or to define modify some coefficients of both sticking efficiency and erosion HAIC models. The latter work is based on an optimization methodology described in this report. Taking the uncertainties into account can improve the numerical predictions, but it is on a case-by-case basis. Concerning the modifications of the HAIC models, the conclusions are not that clear. On one hand, the optimization method has provided improvements on most of the numerical test cases. However, the modification of the coefficients does not seem appropriate, when it comes to the involved physics. Further work is clearly needed either by considering another optimization approach (e.g., different severity functions, different objectives) on the mathematical side, or by improving the modelling by itself on the physics side.

To conclude with the modelling, note that some phenomena have been partially addressed like the water imbibition inside a snow layer, or not addressed at all like the ice shedding and the saltation. These last two aspects were originally planned within the scope of ICE-GENESIS, but have been abandoned following the withdrawal of Russian partners from the project. Future activities in the snow icing should consider these activities.

Lastly, most of the activities conducted during the WP10 and of the derived models have been described in different articles and communications (refer to the Bibliography), thus disseminated through the icing community.

7 Annex

7.1 TUDA snowflake free fall experiment

N	Fall speed m/s	Mass mg	BL Mass mg	d_{Vpro} mm	ρ_{pro} kg/m ³	$\rho_{pro}(BL)$ kg/m ³	Φ_{pro} -	Φ_{pro}^{\perp} -	d_{Vobl} mm	ρ_{obl} kg/m ³	$\rho_{obl}(BL)$ kg/m ³	Φ_{obl} -	Φ_{obl}^{\perp} -	d_{max} mm	ρ_{max} kg/m ³	$\rho_{max}(BL)$ kg/m ³	A_r -
1	0.67	0.063	0.105	1.042	117.0	180.0	0.95	1.05	1.248	64.8	103.2	0.93	1.51	1.505	38.1	62.4	0.34
2	1.83	1.480	0.924	2.571	192.5	100.2	0.95	1.02	3.098	102.1	56.2	0.93	1.51	3.745	55.2	32.4	0.45
3	2.40	16.790	3.907	4.977	265.0	61.1	0.96	1.08	5.880	158.4	36.7	0.95	1.51	6.953	95.4	22.2	0.43
4	1.47	0.576	0.532	2.340	97.2	83.8	0.98	1.47	2.599	65.9	58.1	0.97	1.82	2.898	45.6	41.3	0.47
5	1.49	0.132	0.155	1.143	174.1	195.5	0.98	1.11	1.263	131.1	145.9	0.98	1.35	1.396	99.2	109.3	0.57
6	1.44	0.546	1.217	3.018	40.4	83.6	0.98	1.14	3.369	28.3	59.5	0.98	1.42	3.763	19.9	42.7	0.56
7	1.07	0.170	0.314	1.653	75.1	135.8	0.98	1.09	1.882	51.8	93.2	0.97	1.42	2.144	35.9	64.3	0.49
8	1.80	0.298	0.236	1.493	184.6	138.2	0.97	1.26	1.672	124.2	95.2	0.97	1.56	1.880	86.7	68.3	0.52
9	0.92	0.047	0.085	0.862	188.0	265.7	0.92	0.82	1.075	83.3	127.5	0.90	1.25	1.352	40.8	66.8	0.51
10	1.38	0.243	0.528	2.109	54.7	108.5	0.98	1.12	2.330	38.1	78.0	0.98	1.37	2.583	27.1	57.6	0.56
11	1.69	0.459	0.515	1.994	113.1	125.0	0.97	1.04	2.317	75.6	82.6	0.96	1.39	2.697	51.6	55.7	0.47
12	1.28	0.157	0.191	1.300	168.5	168.0	0.94	0.92	1.591	81.8	87.4	0.92	1.40	1.957	41.2	47.5	0.42
13	1.49	0.134	0.148	1.127	227.4	199.8	0.93	0.87	1.407	109.4	100.4	0.91	1.37	1.766	54.3	52.2	0.57
14	1.64	0.349	0.246	1.487	203.4	143.1	0.98	1.10	1.644	150.9	106.1	0.98	1.35	1.818	112.0	78.7	0.59
15	1.41	0.578	0.582	2.150	178.1	111.2	0.98	1.13	2.386	130.9	81.7	0.98	1.39	2.648	96.2	60.0	0.59
16	1.51	0.266	1.201	3.195	18.5	71.4	0.95	1.15	3.728	10.3	42.5	0.94	1.58	4.391	6.1	27.4	0.36
17	1.21	0.150	0.482	2.017	38.9	114.3	0.97	1.10	2.296	24.1	74.9	0.96	1.43	2.628	15.8	51.7	0.45

Table 3: Experimental and geometrical data for the snowflake free fall experiments

7.2 TUDA and IAG snowflake melting experiment

	Runs	T_a °C	v_a ms ⁻¹	RH -	m_{p0} mg	T_{p0} °C	$t_m \approx t_{circ}$ s	ρ_{p0}^{bulk} kgm ⁻³	C_{i0} -	Φ_{*0} -
Light aggregates	TUDA Run26	24.4	0.6	41	1.578	-14.7	10.7	76	0.32	0.93
	TUDA Run27	28.0	0.7	36	1.711	-14.0	8.7	43	0.20	0.88
	TUDA Run28	25.6	0.6	38	1.575	-16.1	10.3	43	0.14	0.92
	TUDA Run36	26.6	0.7	38	0.449	-14.2	2.9	23	0.20	0.69
	TUDA Run37	28.6	0.6	34	2.046	-14.4	7.9	30	0.15	0.76
	TUDA Run38	28.2	0.6	35	0.487	-13.5	4.4	30	0.17	0.77
	TUDA Run39	28.2	0.5	36	1.652	-13.0	6.2	39	0.18	0.85
	TUDA Run40	27.2	0.6	35	1.187	-15.4	5.5	53	0.18	0.77
	TUDA Run51	28.3	0.7	32	1.059	-13.1	6.3	14	0.09	0.78
	TUDA Run71	25.2	0.5	33	2.057	-16.6	7.9	21	0.12	0.92
	TUDA Run72	26.5	0.6	30	0.964	-15.8	5.3	17	0.14	0.82
Dense aggregates	TUDA Run13	26.0	0.5	26	1.666	-14.0	15.5	112	0.24	0.91
	TUDA Run25	27.4	0.6	35	2.041	-12.5	15.2	120	0.21	0.86
	IAG Run18	28.4	1.0	6	0.723	-7.0	12.8	145	0.36	0.93
	IAG Run27	33.1	0.9	4	0.318	-4.0	6.9	144	0.35	0.88
	IAG Run38	32.4	0.9	1	0.240	-7.0	8.9	132	0.28	0.98

Table 4: Experimental data of snowflake melting

7.3 Current HAIC sticking and erosion models

CSTB database

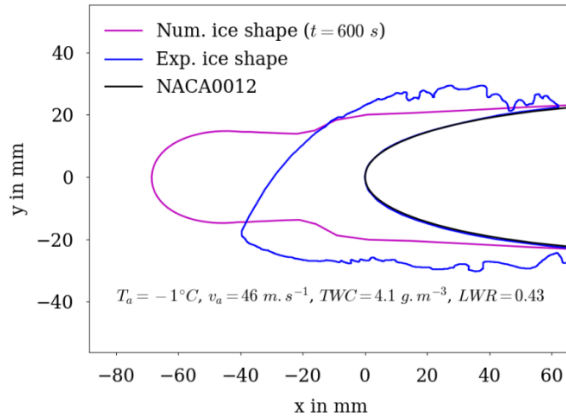


Figure 38: Ice shape comparison for Run401

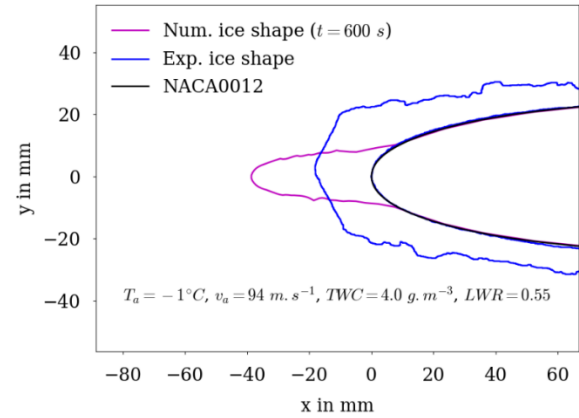


Figure 39: Ice shape comparison for Run901

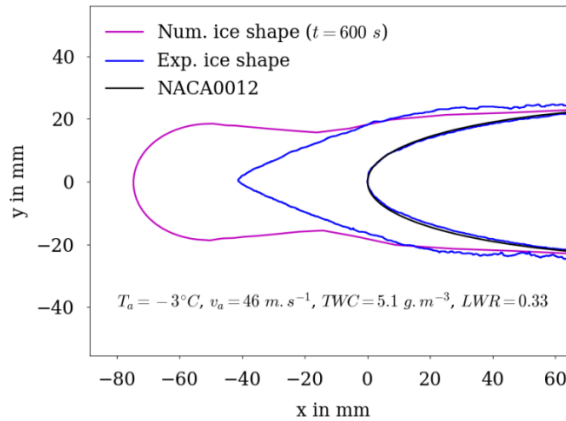


Figure 40: Ice shape comparison for Run403

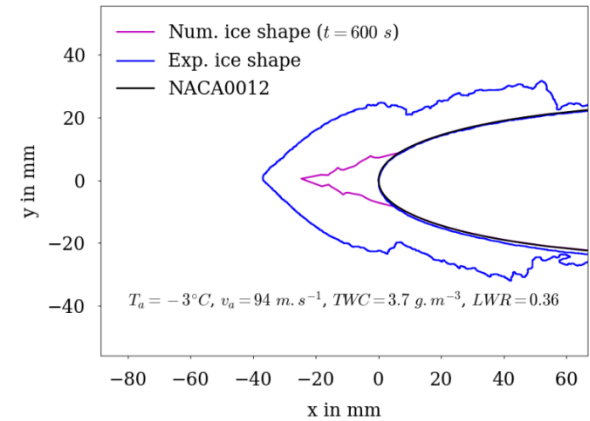


Figure 41: Ice shape comparison for Run903

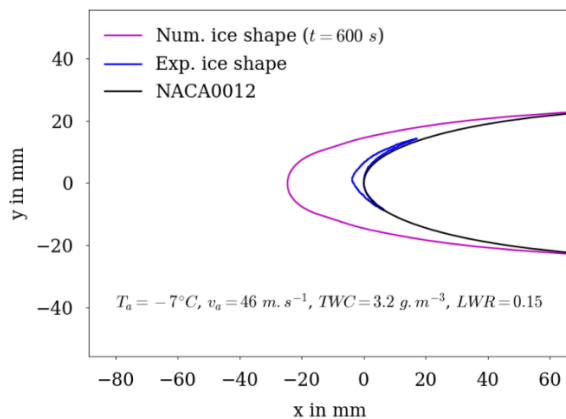


Figure 42: Ice shape comparison for Run407

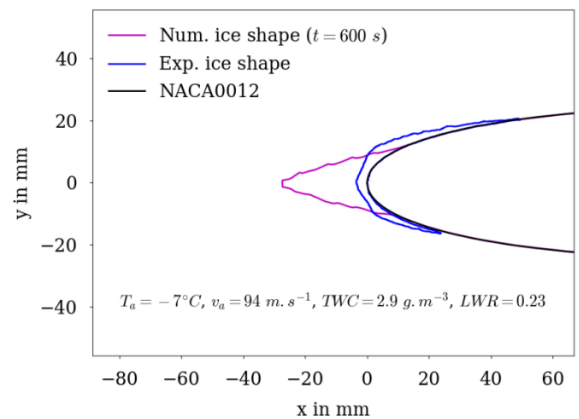


Figure 43: Ice shape comparison for Run907

RTA database

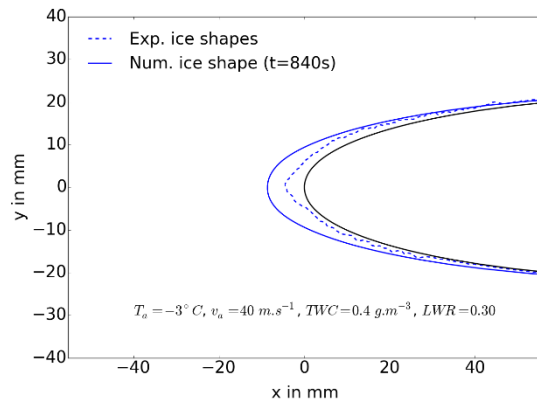


Figure 44: Ice shape comparison for TP14

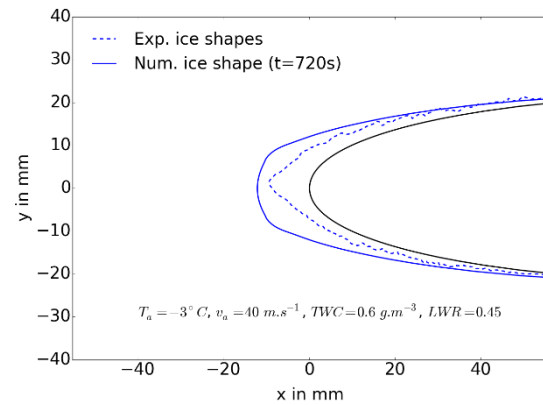


Figure 45: Ice shape comparison for TP15

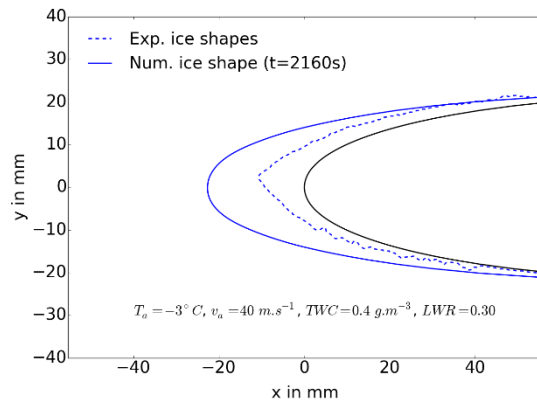


Figure 46: Ice shape comparison for TP19

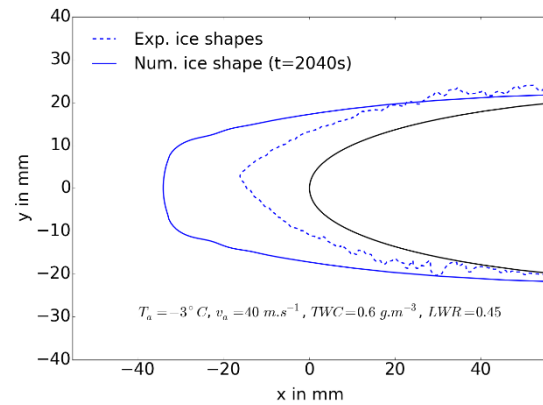


Figure 47: Ice shape comparison for TP20

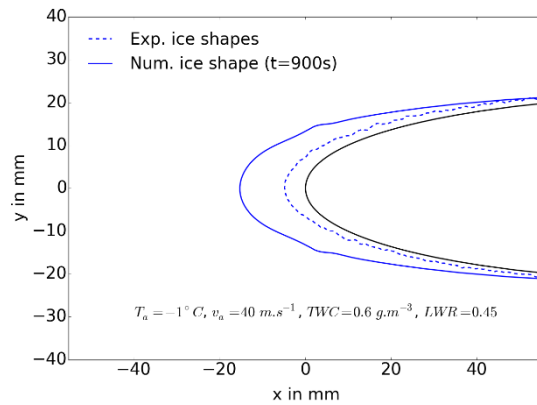


Figure 48: Ice shape comparison for TP21

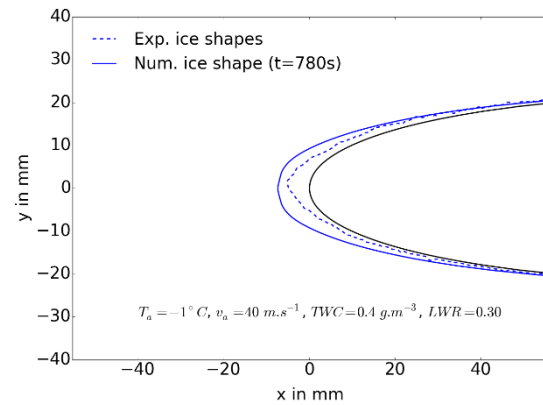


Figure 49: Ice shape comparison for TP22

7.4 Sensitivity numerical results to the measurement uncertainties

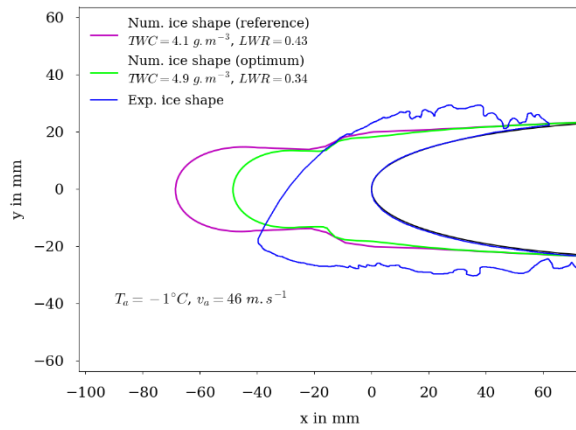


Figure 50: Sensitivity numerical results for Run401

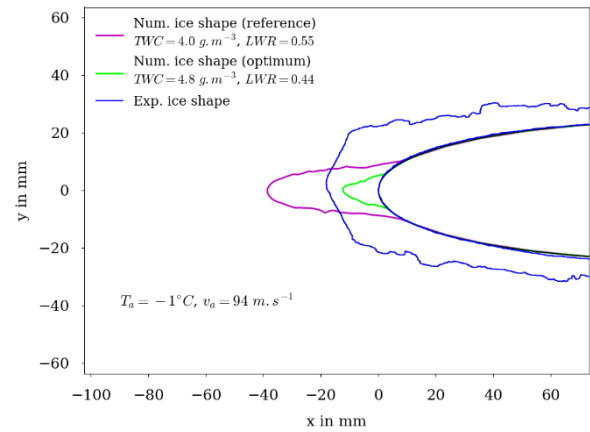


Figure 51: Sensitivity numerical results for Run901

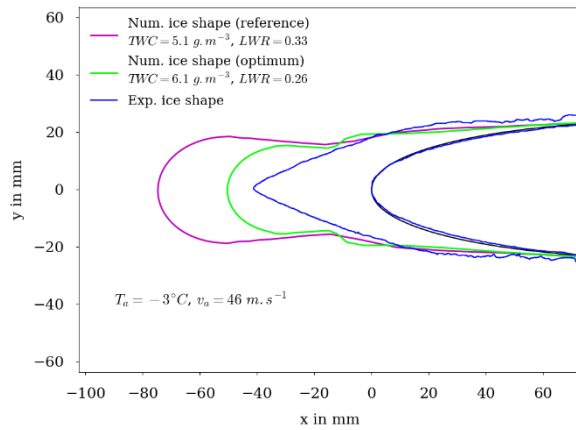


Figure 52: Sensitivity numerical results for Run403

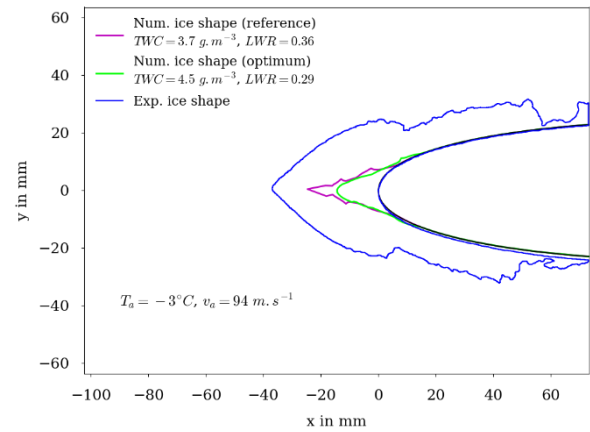


Figure 53: Sensitivity numerical results for Run903

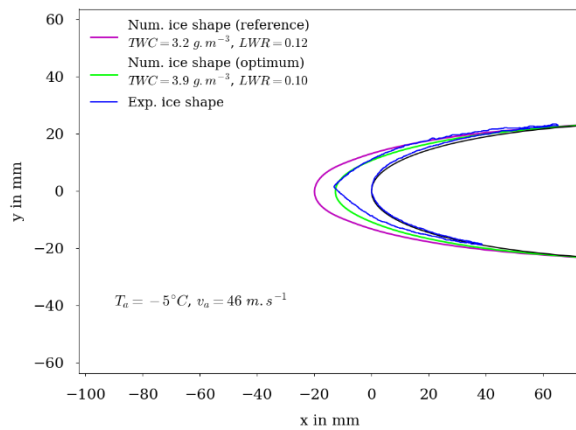


Figure 54: Sensitivity numerical results for Run405

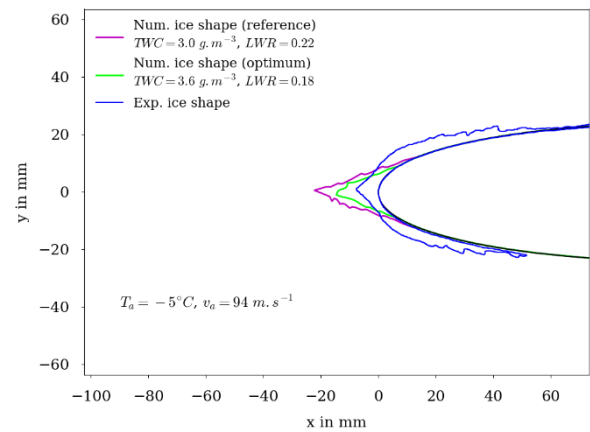


Figure 55: Sensitivity numerical results for Run905

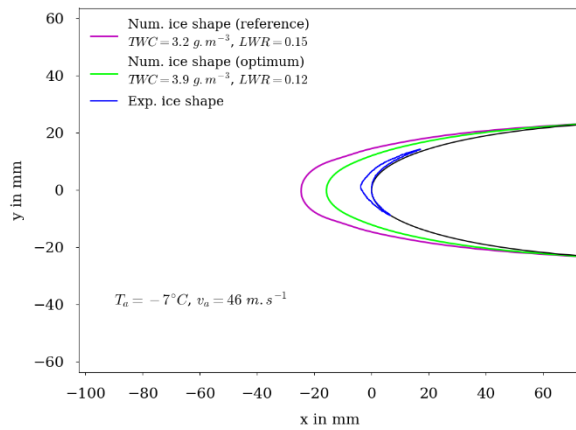


Figure 56: Sensitivity numerical results for Run407

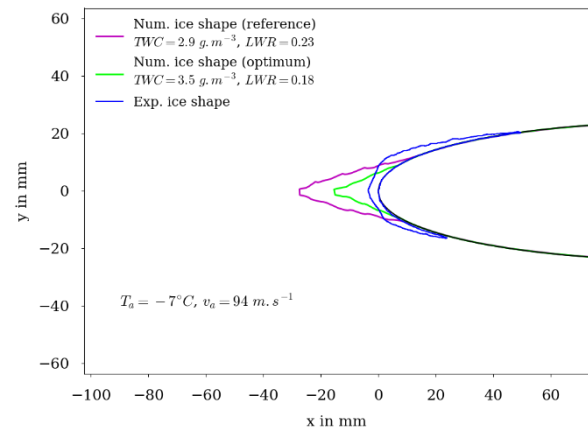


Figure 57: Sensitivity numerical results for Run907

7.5 Optimization study - RTA cases TP07, TP08 and TP09

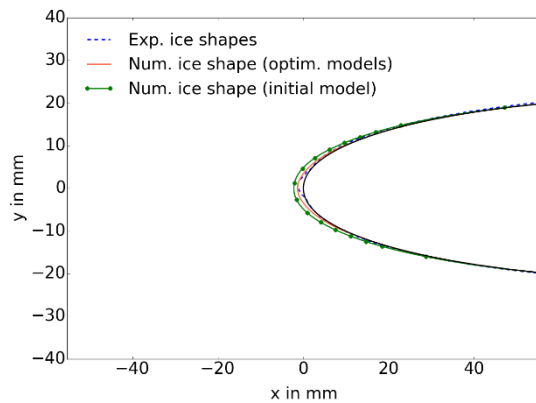


Figure 58: ice shape comparison using mean optimal coefficients in HAIC models and initial HAIC models with the experiment for TP07

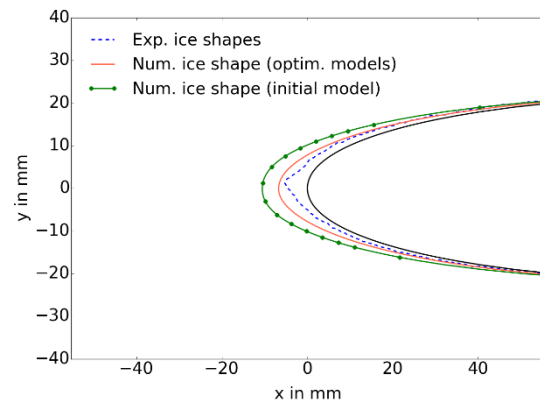


Figure 59: Ice shape using mean optimal coefficients in HAIC models and initial HAIC models with the experiment for TP08

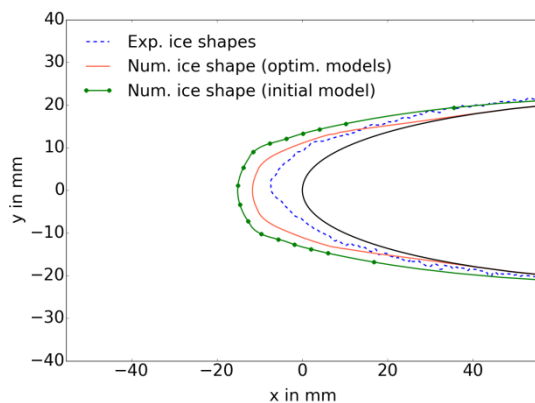


Figure 60: Ice shape using mean optimal coefficients in HAIC models and initial HAIC models with the experiment for TP09

8 Bibliography

- [1] C. Tropea, K. Köbschall and J. Breitenbach, "Ice-Genesis D10.1 - Test Report and Analysis of Advanced snow experimental investigations," 2021.
- [2] O. Rouzaud, "Ice-Genesis D10.2 - Final report on the development of snow models," 2022.
- [3] Q. Duchayne and O. Rouzaud, "Ice-Genesis D10.3 - Final report on the implementation of snow models in 3D icing tools and on the 3D numerical benchmark," 2023.
- [4] A. Hölzer and M. Sommerfeld, "New simple correlation formula for the drag coefficient of non-spherical particles," *Powder Technology*, vol. 184, pp. 361-365, 2008.
- [5] P. Trontin, G. Blanchard and P. Villedieu, "A comprehensive numerical model for mixed-phase and glaciated icing conditions," in *8th AIAA Atmospheric and Space Environments Conference*, 2016.
- [6] T. Hauk, E. Bonaccorso, I. Roisman and C. Tropea, "Ice crystal impact onto a dry solid wall. Particle fragmentation," *Proc. R. Soc. A*, 2015.
- [7] K. Köbschall, J. Breitenbach, I. V. Roisman, C. Tropea and J. Hussong, "Geometric descriptors for the prediction of snowflake drag," *Exp. Fluids*, vol. 64, p. 4, 2022.
- [8] J. D. Locatelli and P. V. Hobbs, "Fall speeds and masses of solid precipitation particles," *Journal of Geophysical Research*, vol. 79, pp. 2185-2197, 1974.
- [9] B. Aguilar, P. Trontin, L. Reitter, K. Köbschall, F. Dezitter, I. Roisman and P. Villedieu, "Ice Crystal Drag Model Extension to Snowflakes: Experimental and Numerical Investigations," *AIAA Journal*, vol. 60, no. 12, pp. 1-14, 2022.
- [10] A. J. Heymsfield and C. Westbrook, "Advances in the estimation of ice particle fall speeds using laboratory and field measurements," *Journal of the Atmospheric Sciences*, vol. 67 (8), pp. 2469-2482, 2010.
- [11] A. Haider and O. Levenspiel, "Drag coefficient and terminal velocity of spherical and nonspherical particles," *Powder Technology*, vol. 58, pp. 63-70, 1989.
- [12] G. H. Ganser, "A rational approach to drag prediction of spherical and nonspherical particles," *Powder Technology*, vol. 77, pp. 143-152, 1993.
- [13] B. Aguilar, "Experimental and numerical investigation of snow accretion.," Ph.D. Thesis, Institut Supérieur de l'Aéronautique et de l'Espace (ISAE), Toulouse, 2024 (to be published).
- [14] F. Dezitter, A. Grandin, J.-L. Berenguier, F. Hervy, H. Schlager, P. Villedieu and G. Zalamansky, "Haic - high altitude ice crystals," in *5th AIAA Atmospheric and Space Environments Conference*, 2013.
- [15] K. Köbschall, B. Traut, I. V. Roisman, C. Tropea and J. Hussong, "Melting of fractal snowflakes: Experiments and modeling," *International Journal of Heat and Mass Transfer*, vol. 212, 2023.
- [16] J. Grazioli, G. Ghiggi, A. C. Billault-Roux and A. Berne, "MASCDB, a database of images, descriptors and microphysical properties of individual snowflakes in free fall.," *Scientific Data*, vol. 9, p. 186, 2022.

- [17] B. Aguilar, P. Trontin, K. Kobschall, F. Dezitter, J. Hussong and P. Villedieu, "Experimental investigation and semi-empirical modelling of snowflake melting," *Journal of Heat and Mass Transfer*, vol. 209, 2023.
- [18] N. Frössling, "Über die verdunstung fallender Tropfen," *Gerlands Beiträge zur Geophysik*, vol. 52, pp. 170-216, 1930.
- [19] S. K. Mitra, O. Vohl, M. Ahr and H. R. Pruppacher, "A wind tunnel and theoretical study of the melting behavior of atmospheric ice particles. IV: Experiment and theory for snow flakes," *Journal of Atmospheric Sciences*, vol. 47, pp. 584-591, 1990.
- [20] W. Wright, P. Jorgenson and J. Veres, "Mixed phase modeling in GlennICE with application to engine icing," in *AIAA Atmospheric and Space Environments Conference*, 2010.
- [21] P. Villedieu, P. Trontin and R. Chauvin, "Glaciated and mixed phase ice accretion modeling using ONERA 2D icing suite," in *6th AIAA atmospheric and space environments conference*, 2014.
- [22] P. Trontin and P. Villedieu, "A comprehensive accretion model for glaciated icing conditions," *International Journal of Multiphase Flow*, vol. 108, p. 105–123, 2018.
- [23] A. Baumert, S. Bansmer, P. Trontin and P. Villedieu, "Experimental and numerical investigations on aircraft icing at mixed phase conditions," *International Journal of Heat and Mass Transfer*, vol. 123, p. 957–978, 2018.
- [24] P. Trontin, A. Kontogiannis, G. Blanchard and P. Villedieu, "Description and assessment of the new ONERA 2D icing suite IGLOO2D.," in *9th AIAA Atmospheric and Space Environments Conference*, 2017.
- [25] G. Gori, A. Raimondi and A. Guardone, "Snowflakes shape characterization via Bayesian inference: exploring the challenges," in *AIAA Aviation Forum*, Online, 2021.
- [26] T. Bellosta, A. Guardone, G. Gori, P. M. Congedo and O. Le Maitre, "Uncertainty quantification for in-flight ice accretion under Appendix-C and Appendix-O conditions," in *AIAA Aviation Forum 2021*, Online, 2021.
- [27] G. Gori, P. M. Congedo, O. Le Maitre, T. Bellosta and A. Guardone, "Modeling In-Flight Ice Accretion Under Uncertain Conditions," *Journal of Aircraft*, vol. 59, no. 13, pp. 799-813, 2021.